JCTC Journal of Chemical Theory and Computation

Article

pubs.acs.org/JCTC

Analytical State-Average Complete-Active-Space Self-Consistent Field Nonadiabatic Coupling Vectors: Implementation with Density-Fitted Two-Electron Integrals and Application to Conical Intersections

Ignacio Fdez. Galván,[*,†,‡] Mickaël G. Delcey,[¶,§] Thomas Bondo Pedersen,[∥] Francesco Aquilante,[⊥] and Roland Lindh[†,‡]

[†]Department of Chemistry—Ångström, The Theoretical Chemistry Programme, and [‡]Uppsala Center for Computational Chemistry—UC_3, Uppsala University, Box 518, 751 20 Uppsala, Sweden

[¶]Chemical Sciences Division, Lawrence Berkeley National Laboratory, Berkeley, California 94720, United States

[§]Kenneth S. Pitzer Center for Theoretical Chemistry, Department of Chemistry, University of California, Berkeley, California 94720, United States

[∥]Centre for Theoretical and Computational Chemistry, Department of Chemistry, University of Oslo, P.O. Box 1033 Blindern, 0315 Oslo, Norway

[⊥]Dipartimento di Chimica "G. Ciamician", Università di Bologna, Via F. Selmi 2, IT-40126 Bologna, Italy

Supporting Information

ABSTRACT: Analytical state-average complete-active-space self-consistent field derivative (nonadiabatic) coupling vectors are implemented. Existing formulations are modified such that the implementation is compatible with Cholesky-based density fitting of two-electron integrals, which results in efficient calculations especially with large basis sets. Using analytical nonadiabatic coupling vectors, the optimization of conical intersections is implemented within the projected constrained optimization method. The standard description and characterization of conical intersections is reviewed and clarified, and a practical and unambiguous system for their classification and interpretation is put forward. These new tools are subsequently tested and benchmarked for 19 different conical intersections. The accuracy of the derivative coupling vectors is validated, and the information that can be drawn from the proposed characterization is discussed, demonstrating its usefulness.

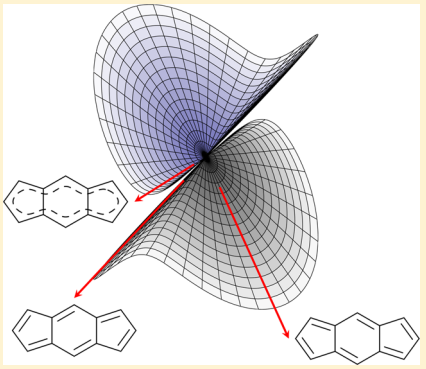

1. INTRODUCTION

The theoretical study of nonadiabatic processes, those in which the nuclear motion involves more than one Born−Oppenheimer potential energy surface, has seen intense development in the last decades. Several reviews on the subject have been published in recent years,[1−6] and the interested reader is encouraged to peruse them and consult references therein. A key quantity in nonadiabatic processes is the derivative coupling vector (also called nonadiabatic coupling vector). It measures the mixing between the adiabatic (Born−Oppenheimer) electronic states with the nuclear motions and, together with the electronic gradient, defines the first-order shape of the potential energy surfaces close to degeneracy regions. Molecular structures with two or more degenerate electronic states are called conical intersections if the degeneracy is lifted linearly with the nuclear displacements.[7−10] The literature on conical intersections, their significance, optimization, and effects on nonadiabatic processes[11] is profuse, in parallel with the development of nonadiabatic theoretical chemistry studies.[12]

In spite of their significance, derivative coupling vectors are often not available from quantum chemistry software packages, as their implementation is not trivial even if one is willing to allow for numerical differentiation. To overcome this limitation, several algorithms have been proposed that obviate the need for the full derivative coupling vector. For example, the fewest-switches surface hopping algorithm for nonadiabatic molecular dynamics[13] requires only the dot product of the derivative coupling and the velocity vector, which is straightforward to evaluate from the wave functions at different timesteps. For the optimization of conical intersections there are also algorithms that do not rely on a derivative coupling vector.[14−16] Nevertheless, analytical formulations have been published for several electronic structure methods,[17−22] and using analytical derivative couplings is almost always preferable to ad hoc numerical differentiation or approximate methods.

Received: April 15, 2016
Published: June 21, 2016

DOI: 10.1021/acs.jctc.6b00384
J. Chem. Theory Comput. 2016, 12, 3636−3653

Molcas[23] is one of the leading software packages when it comes to multiconfigurational methods, due to the efficiency and versatility it offers. However, until now Molcas lacked the ability to compute derivative couplings, analytically or numerically, which limited its potential for use in state-of-the-art applications in the field of nonadiabatic processes. In this work, we address this problem by implementing analytical derivative coupling vectors for state-average complete-active-space self-consistent field (SA-CASSCF) wave functions, the cornerstone of most multiconfigurational calculations with Molcas. Although analytical formulations for general multiconfigurational self-consistent field (MCSCF) and multireference configuration interaction (MRCI) derivative coupling vectors have been published before,[17,19] we simplify the expressions for the specific case of SA-CASSCF and connect them with the formulation for SA-CASSCF energy gradients already used in Molcas.[24]

In the past few years, the performance of Molcas has been greatly improved with the implementation of a Cholesky decomposition scheme for two-electron integrals, its reformulation as a particular form of density fitting, and the exploitation of this in most parts of the code, including analytical derivatives.[25−32] Most of the current development within Molcas takes advantage of this technique, and not doing so for derivative couplings would be a step backward. Devising a general partitioning of the two-particle density matrices, we ensure that our implementation is compatible with density-fitted two-electron integrals.

Regarding the description and characterization of conical intersections, it is our impression that the existing literature has not always succeeded in connecting the formal and mathematical aspects of the phenomenon with the more intuitive and practical consequences. The situation is confusing because, as is natural, different authors have used different formulations, notations and perspectives to describe the intersections. Thus, at the risk of introducing yet another different interpretation, we present here a systematic characterization of conical intersections, providing both a complete and unambiguous mathematical representation of the intersecting surfaces and the branching space, and an identification of the main features likely to determine the system properties. This characterization is done on the basis of local properties (gradients and derivative coupling vectors).

Finally, we extend the projected constrained optimization (PCO) method to locate conical intersections. The PCO method is a general geometry optimization method that can take into account arbitrary constraints, geometrical or not. With the PCO method it is also straightforward to combine additional constraints with those corresponding to the conical intersection, allowing further exploration of the intersection seam.

We have tested these tools by optimizing and characterizing 19 different conical intersection structures on 13 chemical systems. The accuracy of the methods is validated, and the most significant features of the intersections are discussed. The performance gain in using density-fitted two-electron integrals over conventional ones is briefly reported too.

To summarize, the aim of this work is twofold. On the one hand, based on an existing implementation of analytical gradients and including the modifications needed to make it compatible with density fitting, we report and validate an implementation of analytical SA-CASSCF derivative coupling vectors. On the other hand we propose and discuss a consistent, practical, and to some extent intuitive system for characterizing and describing conical intersections, which can be used for analyzing the features of potential energy surfaces.

2. THEORY AND METHODS

This section is split into four subsections. The first is a summary and partial review of the theory of the evaluation of SA-CASSCF derivative coupling vectors. The second subsection deals with the specifics of the efficient evaluation of these coupling vectors in association with a density fitting scheme to represent the two-electron integrals. This is followed by a subsection discussing the characterization of conical intersections. The last subsection deals with the optimization of conical intersections using the projected constrained optimization method.

2.1. Analytical SA-CASSCF Derivative Couplings. Over the last decades, several analytical formulations for computing energy gradients and derivative couplings have been developed for different ab initio methods. It is not our aim to give a complete review on these, but we will simply point out some of the most significant developments for the purpose of this work, which is implementing analytical derivative couplings for SA-MCSCF wave functions (SA-CASSCF in particular) with density fitting.

Page et al.[33] proposed a method to compute gradients for a general multireference configuration interaction (MRCI) wave function, which involved solving the so-called coupled perturbed MCSCF equations, once for each nuclear degree of freedom. Handy and Schaefer[34] showed that, in general, the coupled perturbed equations do not have to be solved for every degree of freedom, but the formulas can be reordered so that the equations can be solved once and the solutions used for all the gradient components. Another highlight was the realization by Rice and Amos[35] that any gradient expression can be calculated from inner products of "effective" density matrices and derivative integrals; these effective density matrices can be efficiently transformed to atomic orbital (AO) basis, avoiding the transformation of the derivative integrals to molecular orbital (MO) basis. Finally, Helgaker and Jørgensen[36] devised a general formulation to obtain derivatives of nonvariational wave functions, by defining a variational Lagrangian function, so that the coupled perturbed equations need not be explicitly invoked; this becomes especially useful for higher derivatives.

These advances allowed Shepard[37] to write the MRCI gradient expression in terms of products of AO densities and integral derivatives, in a formalism that was later extended to MRCI based on SA-MCSCF orbitals.[38,39] For simple SA-MCSCF wave functions, Stålring et al.[24] presented a method based on a Lagrangian formulation, and this is the method implemented in Molcas. The equivalence between the last two results is evident when one compares the equations, considering that in CASSCF the CI and MCSCF spaces are the same, so all orbital rotations within the inactive, active or virtual spaces are redundant, and the quantities labeled with Q or D in ref 39 vanish. The equivalence with the pre-1985 formulation of Page et al.[33] is less obvious, but it can be followed in the above references (and others therein).

The expressions for derivative couplings between MRCI wave functions were shown by Lengsfield et al.[17] to be very similar to those of the gradients, with transition density matrices replacing state density matrices. Using the same techniques developed for the gradients, Lischka et al.[19] expressed the derivative couplings in terms of inner products

DOI: 10.1021/acs.jctc.6b00384
J. Chem. Theory Comput. 2016, 12, 3636−3653

of effective density matrices and AO integral derivatives. Due to the similarity between the gradient formulation in ref 39 and that used in Molcas,[24] we take the corresponding derivative coupling formulation[19] as a basis for this work.

The derivative coupling vector $\boldsymbol{f}^{AB}$ between two states A and B represented by the wave functions $\Psi^A(\boldsymbol{R})$ and $\Psi^B(\boldsymbol{R})$ is defined as

$$f_\alpha^{AB}(\boldsymbol{R}) = \left\langle \Psi^B(\boldsymbol{R}) \middle| \frac{\partial}{\partial R_\alpha} \Psi^A(\boldsymbol{R}) \right\rangle \tag{1}$$

where $\boldsymbol{R}$ is the vector of nuclear coordinates and α is one of its components. The wave functions are expressed as linear combinations of configuration-state functions (CSFs),

$$\Psi^I(\boldsymbol{R}) = \sum_i C_i^I(\boldsymbol{R}) \psi_i(\boldsymbol{R}) \tag{2}$$

and the CSFs ψ_i are linear combinations of Slater determinants of molecular orbitals, which are linear combinations of atom-centered basis functions. For simplicity, the dependence on $\boldsymbol{R}$ will not, in general, be explicitly stated. The vector $\boldsymbol{f}^{AB}$ can be split in two contributions, termed the configuration interaction (CI) contribution and the CSF contribution:

$$f_\alpha^{AB} = {}^{\mathrm{CI}}f_\alpha^{AB} + {}^{\mathrm{CSF}}f_\alpha^{AB} \tag{3}$$

$$\begin{aligned} {}^{\mathrm{CI}}f_\alpha^{AB} &= \left\langle \boldsymbol{C}^B \middle| \frac{\partial}{\partial R_\alpha} \boldsymbol{C}^A \right\rangle = \frac{1}{E^B - E^A} \left\langle \boldsymbol{C}^B \middle| \frac{\partial \mathbf{H}}{\partial R_\alpha} \middle| \boldsymbol{C}^A \right\rangle \\ &= \frac{1}{\Delta E^{AB}} h_\alpha^{AB} \end{aligned} \tag{4}$$

$${}^{\mathrm{CSF}}f_\alpha^{AB} = \sum_{i,j} C_j^B C_i^A \left\langle \psi_j \middle| \frac{\partial}{\partial R_\alpha} \psi_i \right\rangle \tag{5}$$

where $\boldsymbol{C}^I$ is a vector containing the coefficients C_i^I for state I (I = A, B), E^I is the state energy $E^I = \langle \boldsymbol{C}^I | \mathbf{H} | \boldsymbol{C}^I \rangle$, and $\mathbf{H}$ is the Hamiltonian matrix in CSF space $H_{ij} = \langle \psi_i | \hat{H} | \psi_j \rangle$. Although the terms "derivative coupling" and "nonadiabatic coupling" are used as synonyms for $\boldsymbol{f}^{AB}$ in the literature, in this article we will emphasize the difference between $\boldsymbol{f}^{AB}$ and $\boldsymbol{h}^{AB}$ by calling the former "derivative coupling" and the latter "nonadiabatic coupling" and:

$$\boldsymbol{f}^{AB} = \frac{\boldsymbol{h}^{AB}}{\Delta E^{AB}} + {}^{\mathrm{CSF}}\boldsymbol{f}^{AB} \tag{6}$$

In an SA-MCSCF calculation, the CI coefficients for each state, $\boldsymbol{C}^I$, are obtained by diagonalization of $\mathbf{H}$, while the orbital coefficients that define the CSFs and thus $\mathbf{H}$ result from minimization of the state-averaged energy

$$E^{\mathrm{SA}} = \sum_{I \in \mathrm{SA}} w_I \langle \boldsymbol{C}^I | \mathbf{H} | \boldsymbol{C}^I \rangle \tag{7}$$

with respect to orbital rotations. The factor w_I is the weight assigned to state I in the average. An SA-CASSCF calculation is a special case of SA-MCSCF where the CSFs are all the possible excitations within a preselected set of orbitals.

The nonadiabatic coupling can be computed by first solving the coupled perturbed SA-MCSCF equations, which in the case of equal-weights SA can be written as

$$\begin{pmatrix} \mathbf{G}^{\mathrm{orb,orb}} & \mathbf{G}^{\mathrm{orb,CI}} \\ \mathbf{G}^{\mathrm{CI,orb}} & \mathbf{G}^{\mathrm{CI,CI}} \end{pmatrix} \begin{pmatrix} \boldsymbol{\lambda}^{\mathrm{orb}} \\ \boldsymbol{\lambda}^{\mathrm{CI}} \end{pmatrix} = \begin{pmatrix} \boldsymbol{L}^{\mathrm{orb}} \\ \mathbf{0} \end{pmatrix} \tag{8}$$

where $\mathbf{G}$ is the usual electronic Hessian matrix, the second derivative of the SA-MCSCF energy with respect to the wave function parameters ("orb" orbital rotations; "CI" CI expansion coefficients); $\boldsymbol{\lambda}$ are the solutions to the system of equations; $\boldsymbol{L}^{\mathrm{orb}}$ has components

$$L_{(pq)} = 2(F_{pq}^{AB} - F_{qp}^{AB}) \tag{9}$$

$$F_{pq}^{AB} = \sum_o D_{po}^{AB} h_{qo} + \sum_{r,s,o} d_{prso}^{AB} g_{qrso} \tag{10}$$

with (pq) as a compound index referring only to the unique elements of the nonredundant orbital rotation matrix. In particular, the compound index does not contain rotations within the active space (both p and q active). The Fock matrix $\mathbf{F}^{AB}$ is computed from the one- (h) and two-electron (g) integrals, and the symmetric transition density matrices $\mathbf{D}^{AB}$ and $\mathbf{d}^{AB}$.[40]

The solutions $\boldsymbol{\lambda}$ are employed in defining auxiliary density matrices

$$\Lambda_{pq}^{\mathrm{orb}} = -\Lambda_{qp}^{\mathrm{orb}} = \lambda_{(pq)}^{\mathrm{orb}} \tag{11}$$

$$D_{pq}^{\mathrm{orb}} = w \sum_o (\Lambda_{op}^{\mathrm{orb}} D_{oq}^{\mathrm{SA}} + \Lambda_{oq}^{\mathrm{orb}} D_{po}^{\mathrm{SA}}) \tag{12}$$

$$d_{pqrs}^{\mathrm{orb}} = w \sum_o (\Lambda_{op}^{\mathrm{orb}} d_{oqrs}^{\mathrm{SA}} + \Lambda_{oq}^{\mathrm{orb}} d_{pors}^{\mathrm{SA}} + \Lambda_{or}^{\mathrm{orb}} d_{pqos}^{\mathrm{SA}} + \Lambda_{os}^{\mathrm{orb}} d_{pqro}^{\mathrm{SA}}) \tag{13}$$

$$\langle K| = \sum_i C_i^K \psi_i; \qquad \langle K^{\mathrm{CI}}| = \sum_i \lambda_{Ki}^{\mathrm{CI}} \psi_i \tag{14}$$

$$D_{pq}^{\mathrm{CI}} = w \sum_{K \in \mathrm{SA}} \langle K | \hat{E}_{pq} + \hat{E}_{qp} | K^{\mathrm{CI}} \rangle \tag{15}$$

$$d_{pqrs}^{\mathrm{CI}} = w \frac{1}{2} \sum_{K \in \mathrm{SA}} \langle K | \hat{e}_{pqrs} + \hat{e}_{pqsr} + \hat{e}_{qprs} + \hat{e}_{qpsr} | K^{\mathrm{CI}} \rangle \tag{16}$$

where $\mathbf{D}^{\mathrm{SA}}$ and $\mathbf{d}^{\mathrm{SA}}$ are the state-averaged density matrices, w is the weight used in the state average (the same for all states K), and $\hat{E}_{st}$, $\hat{e}_{stuv}$ are the standard one- and two-electron excitation operators of second quantization.[41]

Once these matrices are obtained, the nonadiabatic coupling can be computed from the effective density matrices

$$\mathbf{D}^{\mathrm{eff}} = \mathbf{D}^{AB} + \mathbf{D}^{\mathrm{orb}} + \mathbf{D}^{\mathrm{CI}} \tag{17}$$

$$\mathbf{d}^{\mathrm{eff}} = \mathbf{d}^{AB} + \mathbf{d}^{\mathrm{orb}} + \mathbf{d}^{\mathrm{CI}} \tag{18}$$

$$h_\alpha^{AB} = \mathbf{h}^\alpha : \mathbf{D}^{\mathrm{eff}} + \frac{1}{2} \mathbf{g}^\alpha : \mathbf{d}^{\mathrm{eff}} - \mathbf{S}^\alpha : \mathbf{F}^{\mathrm{eff}} \tag{19}$$

where $\mathbf{h}^\alpha$, $\mathbf{g}^\alpha$, and $\mathbf{S}^\alpha$ are the derivatives of the one- and two-electron integrals and of the overlap integrals, respectively, $\mathbf{F}^{\mathrm{eff}}$ is an effective Fock matrix, computed as in eq 10, but with the effective density matrices $\mathbf{D}^{\mathrm{eff}}$ and $\mathbf{d}^{\mathrm{eff}}$. The notation $\mathbf{X}$:$\mathbf{Y}$ indicates the Frobenius inner product of matrices $\mathbf{X}$ and $\mathbf{Y}$,

$$\mathbf{X} : \mathbf{Y} = \mathrm{Tr}(\mathbf{X}^{\mathrm{T}} \mathbf{Y}) = \sum_{\mu,\nu} X_{\mu\nu} Y_{\mu\nu} \tag{20}$$

In eq 19 it is assumed that all quantities are expressed in AO basis.

DOI: 10.1021/acs.jctc.6b00384
J. Chem. Theory Comput. 2016, 12, 3636−3653

These expressions differ from ref 19 only in that quantities there labeled with D or Q, are set to zero, due to the MCSCF and CI spaces being the same in SA-CASSCF (no orbital subspaces need be resolved). Furthermore, these expressions are identical to those implemented in Molcas for SA-MCSCF gradients,[24] with transition density matrices replacing state density matrices in the equivalent of eqs 10, 17, and 18, both for conventional and density-fitted two-electron integrals.[32]

The ${}^{\mathrm{CSF}}\boldsymbol{f}^{AB}$ component, eq 5, can be computed in AO basis as

$$ {}^{\mathrm{CSF}}f_{\alpha}^{AB} = 2\mathbf{S}^{\alpha,-} : \mathbf{D}^{AB,-} \tag{21} $$

where $\mathbf{D}^{AB,-}$ is the antisymmetric component of the one-electron transition density matrix and $\mathbf{S}^{\alpha,-}$ is the antisymmetric derivative overlap

$$ S_{\mu\nu}^{\alpha,-} = \frac{1}{2}\left(\left\langle \chi_\mu \middle| \frac{\partial}{\partial R_\alpha}\chi_\nu \right\rangle - \left\langle \frac{\partial}{\partial R_\alpha}\chi_\mu \middle| \chi_\nu \right\rangle \right) \tag{22} $$

with χ_μ being the atomic basis functions. Here again, this simplifies the expression in ref 19, which includes an additional term that can be incorporated by modifying eq 8. However, this term can be shown to vanish in a CASSCF calculation, since the orbital subspaces need not be resolved, and, in MO basis, $D_{pq}^{AB,-} = 0$ if p and q are not both active orbitals.

When studying nonadiabatic processes, e.g. with "surface hopping" molecular dynamics simulations, the full derivative coupling (eq 6) is needed. But $\boldsymbol{f}^{AB}$ is undefined at conical intersection points ($\Delta E^{AB} = 0$), and for locating and characterizing these, the quantity of interest is $\boldsymbol{h}^{AB}$, which together with the difference gradient defines the branching space (see section 2.3). In addition, ${}^{\mathrm{CSF}}\boldsymbol{f}^{AB}$, is not translation/rotation invariant even in the absence of an external potential.[17] This lack of invariance can lead to unphysical results in dynamics studies, and it is due to the absence of electron momentum in the Born−Oppenheimer approximation.[21] Fatehi et al.[21] have addressed this problem by including electron translation factors in the AO level, which results in a very simple recipe to restore translational invariance: set $\mathbf{S}^{\alpha,-} = 0$.[21,42,43] In the present case, this correction means simply ignoring ${}^{\mathrm{CSF}}\boldsymbol{f}^{AB}$. Thus, for most practical applications, only $\boldsymbol{h}^{AB}$ is required.

2.2. Implementation. The implementation of SA-CASSCF derivative couplings with density fitting in Molcas follows closely that of SA-CASSCF gradients,[24,32] the only difference appears in the partitioning of the two-electron density matrices, and in the computation of ${}^{\mathrm{CSF}}\boldsymbol{f}^{AB}$. All other details regarding the use of density-fitted two-electron integrals in ref 32 remain valid and we will not be concerned with them here.

In eq 19 the effective two-electron density matrix in AO basis, $\mathbf{d}^{\mathrm{eff}}$, is needed, but its size increases with the fourth power of the number of basis functions, so it is not practical to store it fully. Instead, only the contribution from the active orbitals (in MO basis) is stored and the full matrix is reconstructed on the fly employing the following partitioning.

Using the notation

$$ [\mathbf{X}, \mathbf{Y}]_{pqrs} = [\mathbf{Y}, \mathbf{X}]_{pqrs} = X_{pq}Y_{rs} + Y_{pq}X_{rs} - \frac{1}{2}(X_{ps}Y_{qr} + Y_{ps}X_{qr}) \tag{23} $$

a symmetric MCSCF two-electron density matrix can be partitioned into its active-only part $\mathbf{d}^{\mathrm{A}}$ and a part obtainable from one-electron density matrices:

$$ d_{pqrs} = d_{pqrs}^{\mathrm{A}} + \left[\mathbf{D}^{\mathrm{D}}, \frac{1}{2}\mathbf{D}^{\mathrm{I}} + \mathbf{D}^{\mathrm{A}} \right]_{pqrs} \tag{24} $$

where $\mathbf{D}^{\mathrm{I}}$ and $\mathbf{D}^{\mathrm{A}}$ are, respectively, the inactive and active components of the one-electron density matrix ($\mathbf{D} = \mathbf{D}^{\mathrm{I}} + \mathbf{D}^{\mathrm{A}}$), and $\mathbf{D}^{\mathrm{D}}$ is a matrix with 2 in its inactive diagonal elements and 0 elsewhere (in MO basis). In a state density matrix, $\mathbf{D}^{\mathrm{I}} = \mathbf{D}^{\mathrm{D}}$, while in a transition density matrix $\mathbf{D}^{\mathrm{I}} = \mathbf{0}$ and $\mathbf{D}^{\mathrm{A}} = \mathbf{D}$. This partitioning cannot be applied to $\mathbf{d}^{\mathrm{eff}}$ directly, but it can be applied to the auxiliary density matrices $\mathbf{d}^{\mathrm{orb}}$ and $\mathbf{d}^{\mathrm{CI}}$. The matrix $\mathbf{d}^{\mathrm{CI}}$ has the form of a transition density matrix, even when computing a gradient, since it involves two orthogonal CI vectors (eq 16):

$$ d_{pqrs}^{\mathrm{CI}} = d_{pqrs}^{\mathrm{CI,A}} + \left[\mathbf{D}^{\mathrm{D}}, \frac{1}{2}\mathbf{D}^{\mathrm{CI,I}} + \mathbf{D}^{\mathrm{CI,A}} \right]_{pqrs} \tag{25} $$

$$ = d_{pqrs}^{\mathrm{CI,A}} + [\mathbf{D}^{\mathrm{D}}, \mathbf{D}^{\mathrm{CI}}]_{pqrs} \tag{26} $$

while $\mathbf{d}^{\mathrm{orb}}$ is a one-index-transformed state (averaged) density matrix, even when computing nonadiabatic couplings. Using the notation $\{\mathbf{X}\}^{\Lambda}$ for the one-index transformations in eqs 12 and 13, such that

$$ D_{pq}^{\mathrm{orb}} = \{\mathbf{D}^{\mathrm{SA}}\}_{pq}^{\Lambda} \tag{27} $$

$$ d_{pqrs}^{\mathrm{orb}} = \{\mathbf{d}^{\mathrm{SA}}\}_{pqrs}^{\Lambda} \tag{28} $$

$$ \{[\mathbf{X}, \mathbf{Y}]\}_{pqrs}^{\Lambda} = [\{\mathbf{X}\}^{\Lambda}, \mathbf{Y}]_{pqrs} + [\mathbf{X}, \{\mathbf{Y}\}^{\Lambda}]_{pqrs} \tag{29} $$

then $\mathbf{d}^{\mathrm{orb}}$ can be partitioned as

$$ \begin{aligned} d_{pqrs}^{\mathrm{orb}} &= \{\mathbf{d}^{\mathrm{SA,A}}\}_{pqrs}^{\Lambda} + \left\{ \left[\mathbf{D}^{\mathrm{D}}, \frac{1}{2}\mathbf{D}^{\mathrm{SA,I}} + \mathbf{D}^{\mathrm{SA,A}} \right] \right\}_{pqrs}^{\Lambda} \\ &= d_{pqrs}^{\mathrm{orb,A}} + \frac{1}{2}\{[\mathbf{D}^{\mathrm{D}}, \mathbf{D}^{\mathrm{D}}]\}_{pqrs}^{\Lambda} + \{[\mathbf{D}^{\mathrm{D}}, \mathbf{D}^{\mathrm{SA,A}}]\}_{pqrs}^{\Lambda} \\ &= d_{pqrs}^{\mathrm{orb,A}} + [\mathbf{D}^{\mathrm{D}}, \{\mathbf{D}^{\mathrm{D}}\}^{\Lambda}]_{pqrs} + [\{\mathbf{D}^{\mathrm{D}}\}^{\Lambda}, \mathbf{D}^{\mathrm{SA,A}}]_{pqrs} \\ &\quad + [\mathbf{D}^{\mathrm{D}}, \{\mathbf{D}^{\mathrm{SA,A}}\}^{\Lambda}]_{pqrs} \\ &= d_{pqrs}^{\mathrm{orb,A}} + [\mathbf{D}^{\mathrm{D}}, \mathbf{D}^{\mathrm{orb,I}}]_{pqrs} + [\mathbf{D}^{\mathrm{orb,I}}, \mathbf{D}^{\mathrm{SA,A}}]_{pqrs} \\ &\quad + [\mathbf{D}^{\mathrm{D}}, \mathbf{D}^{\mathrm{orb,A}}]_{pqrs} \\ &= d_{pqrs}^{\mathrm{orb,A}} + [\mathbf{D}^{\mathrm{D}}, \mathbf{D}^{\mathrm{orb}}]_{pqrs} + [\mathbf{D}^{\mathrm{SA,A}}, \mathbf{D}^{\mathrm{orb,I}}]_{pqrs} \end{aligned} \tag{30} $$

and finally, the effective two-electron density matrix:

$$ d_{pqrs}^{\mathrm{eff,A}} = d_{pqrs}^{\mathrm{A}} + d_{pqrs}^{\mathrm{orb,A}} + d_{pqrs}^{\mathrm{CI,A}} \tag{31} $$

$$ \begin{aligned} d_{pqrs}^{\mathrm{eff}} &= d_{pqrs}^{\mathrm{eff,A}} + \left[\mathbf{D}^{\mathrm{D}}, \frac{1}{2}\mathbf{D}^{\mathrm{I}} + \mathbf{D}^{\mathrm{A}} + \mathbf{D}^{\mathrm{orb}} + \mathbf{D}^{\mathrm{CI}} \right]_{pqrs} \\ &\quad + [\mathbf{D}^{\mathrm{SA,A}}, \mathbf{D}^{\mathrm{orb,I}}]_{pqrs} \\ &= d_{pqrs}^{\mathrm{eff,A}} + \left[\mathbf{D}^{\mathrm{D}}, \mathbf{D}^{\mathrm{eff}} - \frac{1}{2}\mathbf{D}^{\mathrm{I}} \right]_{pqrs} + [\mathbf{D}^{\mathrm{SA,A}}, \mathbf{D}^{\mathrm{orb,I}}]_{pqrs} \end{aligned} \tag{32} $$

DOI: 10.1021/acs.jctc.6b00384
J. Chem. Theory Comput. 2016, 12, 3636−3653

The matrix $\mathbf{D}^{\mathrm{D}}$ is trivial, and so is $\mathbf{D}^{\mathrm{eff}} - \frac{1}{2}\mathbf{D}^{\mathrm{I}}$ once $\mathbf{D}^{\mathrm{eff}}$ is known (in fact, for nonadiabatic couplings this is just $\mathbf{D}^{\mathrm{eff}}$), $\mathbf{D}^{\mathrm{SA,A}}$ is obtained directly from the SA-CASSCF calculation, and $\mathbf{D}^{\mathrm{orb},I}$ is the one-index transformation of $\mathbf{D}^{\mathrm{D}}$.

This partitioning, unlike that used in ref 24, is valid for both state and transition density matrices, with their appropriate values for $\mathbf{D}^{\mathrm{I}}$, and it is in fact similar to the partitioning proposed in ref 32 for evaluation of the exchange component. In our current implementation we use exclusively the partitioning in eq 32 throughout, for gradients and nonadiabatic couplings, with conventional two-electron integrals or with density-fitted integrals.

The ${}^{\mathrm{CSF}}\boldsymbol{f}^{AB}$ component, eq 21, does not appear in the gradients. Its calculation is trivial and does not even require explicitly building $\mathbf{S}^{\alpha,-}$. Let us first consider the normal connection term present in all gradient expressions, as in eq 19:

$$\mathbf{S}^{\alpha} : \mathbf{F} = \sum_{\mu,\nu} S^{\alpha}_{\mu\nu} F_{\mu\nu} \tag{33}$$

The matrix $\mathbf{S}^{\alpha}$ is symmetric, the sum of left and right derivatives, which are transposes of one another:

$$\begin{aligned} S^{\alpha}_{\mu\nu} &= \left\langle \chi_\mu \middle| \frac{\partial}{\partial R_\alpha} \chi_\nu \right\rangle + \left\langle \frac{\partial}{\partial R_\alpha} \chi_\mu \middle| \chi_\nu \right\rangle \\ &= S^{\mathrm{R}\alpha}_{\mu\nu} + S^{\mathrm{L}\alpha}_{\mu\nu} \\ &= S^{\mathrm{R}\alpha}_{\mu\nu} + S^{\mathrm{R}\alpha}_{\nu\mu} \end{aligned} \tag{34}$$

The only nonzero elements of $\mathbf{S}^{\alpha}$, and the only contributions to eq 33, are for those pairs where either χ_μ or χ_ν is centered on the atom affected by α. If both functions are centered on the same atom, $S^{\mathrm{R}\alpha}_{\mu\nu} = -S^{\mathrm{R}\alpha}_{\nu\mu}$ and $S^{\alpha}_{\mu\nu} = 0$, and if only χ_μ (χ_ν) is centered on the α atom, $S^{\mathrm{R}\alpha}_{\mu\nu} = 0$ ($S^{\mathrm{R}\alpha}_{\nu\mu} = 0$). In addition, if χ_μ is centered on α and χ_ν is centered on β, $S^{\alpha}_{\mu\nu} = -S^{\beta}_{\mu\nu}$. Thus, eq 33 can be computed by evaluating, for each α, only the nonzero $S^{\mathrm{R}\alpha}_{\mu\nu}$, and adding the contribution, with opposite sign, to the β component of the gradient.

The appearance of the antisymmetric $\mathbf{S}^{\alpha,-}$ in the expression for ${}^{\mathrm{CSF}}\boldsymbol{f}^{AB}$ makes it slightly different, but it still can be computed in a similar fashion, evaluating each nonzero $S^{\mathrm{R}\alpha}_{\mu\nu}$ only once, since

$$S^{\alpha,-}_{\mu\nu} = \frac{1}{2}(S^{\mathrm{R}\alpha}_{\mu\nu} - S^{\mathrm{R}\alpha}_{\nu\mu}) \tag{35}$$

but now $S^{\alpha,-}_{\mu\nu} = S^{\beta,-}_{\mu\nu}$, with no change of sign, and $S^{\alpha,-}_{\mu\nu} \neq 0$ if both χ_μ and χ_ν belong to the α atom. And these are, in practice, the only differences in the algorithm if $S^{\mathrm{R}\alpha}_{\mu\nu}$ is used directly as outlined above.

2.3. Conical Intersection Characterization. At a conical intersection point, two electronic states A and B are degenerate ($E^A = E^B$) and the degeneracy is lifted linearly by distortions of the nuclear geometry in two independent directions, which form the *branching space* or *branching plane*. In all the other directions the degeneracy is maintained to first order, and they form the *intersection space*. In the nonrelativistic approximation, conical intersections occur only between states of the same spin multiplicity. The following discussion is based on previous works on conical intersections, especially on refs 10, 12, and 44; the notation has been standardized and the interpretation has been expanded and unified.

The energies of the two intersecting states in the vicinity of a conical intersection can be approximated to first order by means of the three vectors $\boldsymbol{g}^A$, $\boldsymbol{g}^B$ (the gradients of the two states) and $\boldsymbol{h}^{AB}$ (the nonadiabatic coupling between the two states), all computed at the intersection point.[10,12] Instead of $\boldsymbol{g}^A$, $\boldsymbol{g}^B$, it is more convenient to use their sum and difference:

$$\boldsymbol{g}^{AB} = \frac{1}{2}(\boldsymbol{g}^B - \boldsymbol{g}^A) \tag{36}$$

$$\boldsymbol{s}^{AB} = \frac{1}{2}(\boldsymbol{g}^B + \boldsymbol{g}^A) \tag{37}$$

so that the branching plane is defined by the vectors $\boldsymbol{g}^{AB}$ and $\boldsymbol{h}^{AB}$. These latter vectors are not uniquely defined, because the two states are degenerate and any linear combination of them can be chosen, which determines the particular pair of vectors that will be obtained. The term $\boldsymbol{s}^{AB}$, on the contrary, is invariant to the specific choice of the electronic states. Moreover, $\boldsymbol{s}^{AB}$ will in general not be contained in the branching plane but will have a component in the intersection space. Attending to this component, singular intersection points can be identified, such as minimum-energy conical intersection points (MECIs), where the energy of the intersecting states is at a local minimum in the intersection space. At a MECI, $\boldsymbol{s}^{AB}$ is completely contained in the branching plane. The rest of this section is valid for arbitrary intersection points.

A rotation of the two intersecting states (their CI vectors) by an angle $\frac{1}{2}\beta$ causes the following transformation in the corresponding $\boldsymbol{g}^{AB}$ and $\boldsymbol{h}^{AB}$ vectors:

$$\tilde{\boldsymbol{g}} = \boldsymbol{g}^{AB} \cos\beta + \boldsymbol{h}^{AB} \sin\beta \tag{38}$$

$$\tilde{\boldsymbol{h}} = \boldsymbol{h}^{AB} \cos\beta - \boldsymbol{g}^{AB} \sin\beta \tag{39}$$

It is then possible to select the angle β such that the resulting $\tilde{\boldsymbol{g}}$ and $\tilde{\boldsymbol{h}}$ vectors are orthogonal, by setting

$$\tan 2\beta = \frac{2\boldsymbol{g}^{AB}\cdot\boldsymbol{h}^{AB}}{\boldsymbol{g}^{AB}\cdot\boldsymbol{g}^{AB} - \boldsymbol{h}^{AB}\cdot\boldsymbol{h}^{AB}} \tag{40}$$

There are still four nonequivalent angles that satisfy this condition, and they correspond to additional $\frac{\pi}{2}$ rotations of the $\tilde{\boldsymbol{g}}$ and $\tilde{\boldsymbol{h}}$ vectors, i.e., the two vectors can be interchanged with adequate rotations of the electronic states, and they do not have a fixed role. To make this clear, we change the notation to $\boldsymbol{x}$ and $\boldsymbol{y}$, and we denote the orthogonal and normalized vectors that define the branching plane as $\hat{\boldsymbol{x}}$ and $\hat{\boldsymbol{y}}$:

$$\hat{\boldsymbol{x}} = \frac{\tilde{\boldsymbol{g}}}{\sqrt{\tilde{\boldsymbol{g}}\cdot\tilde{\boldsymbol{g}}}}; \qquad \hat{\boldsymbol{y}} = \frac{\tilde{\boldsymbol{h}}}{\sqrt{\tilde{\boldsymbol{h}}\cdot\tilde{\boldsymbol{h}}}} \tag{41}$$

The orthogonalization achieved in this way has the desirable properties of being symmetry-adapted, independent of the initial choice of the $\boldsymbol{g}^{AB}$ and $\boldsymbol{h}^{AB}$ vectors, and continuous along an intersection seam.[45] It is also noteworthy that the vectors $\tilde{\boldsymbol{g}}$ and $\tilde{\boldsymbol{h}}$ are not just arbitrary rotations of $\boldsymbol{g}^{AB}$ and $\boldsymbol{h}^{AB}$ but are the pair of vectors that would result from an appropriate unitary rotation of the wave functions at the conical intersection. Since at an intersection the two wave functions can be arbitrarily rotated, there is no loss of information in this orthogonalization.

Geometries in the branching plane can thus be defined as

$$\boldsymbol{R}(x, y) = \boldsymbol{R}^{\times} + x\hat{\boldsymbol{x}} + y\hat{\boldsymbol{y}} \tag{42}$$

DOI: 10.1021/acs.jctc.6b00384
J. Chem. Theory Comput. 2016, 12, 3636−3653

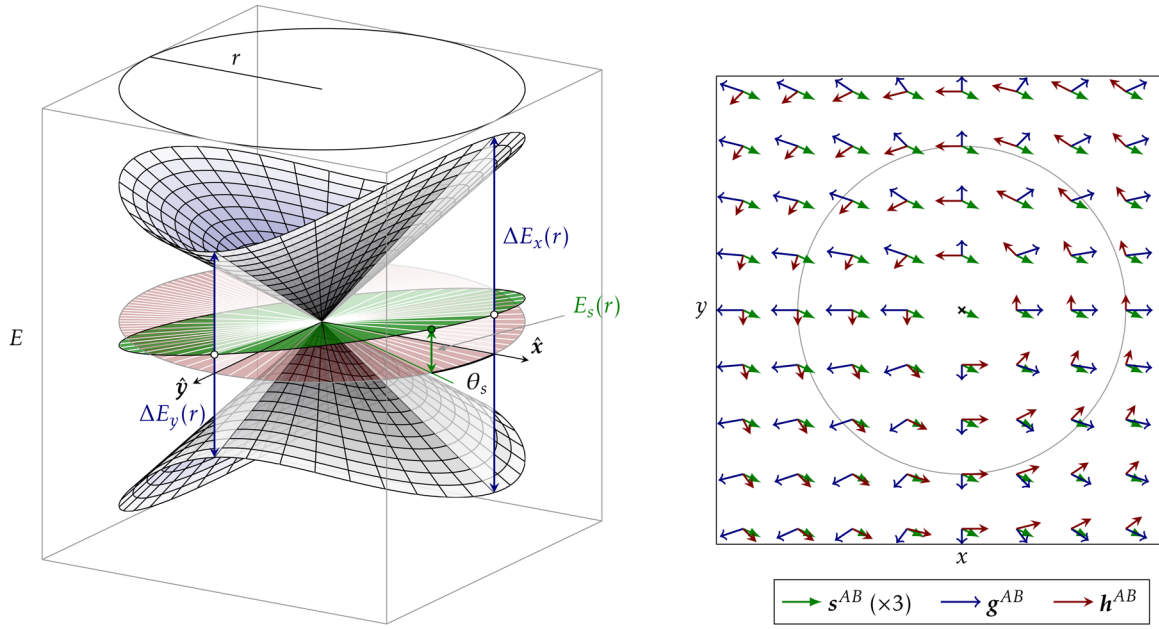

$$\delta_{gh} = \sqrt{\frac{\Delta E_x(r)^2 + \Delta E_y(r)^2}{8r^2}} \qquad \Delta_{gh} = \frac{\Delta E_x(r)^2 - \Delta E_y(r)^2}{\Delta E_x(r)^2 + \Delta E_y(r)^2} \qquad \sigma = \frac{E_s(r)}{\delta_{gh} r}$$

Figure 1. Electronic surfaces around a conical intersection in the branching plane, with characteristic parameters labeled. The vectors $\hat{\boldsymbol{x}}$ and $\hat{\boldsymbol{y}}$ define the branching plane. At a given distance from the intersection r, $\Delta E_x(r)$ and $\Delta E_y(r)$ are the energy differences between the two states, on the x and y directions; the pitch δ_{gh} is related to their sum and can be seen simply as a scale factor, the asymmetry Δ_{gh} is related to their difference. The average energy forms a plane (green), tilted with respect to the xy plane (red), its maximum at the distance r, $E_s(r)$, is found at an angle θ_s and defines the relative tilt σ. The right plot represents the three vectors that describe the intersection in the branching plane.

where $\boldsymbol{R}^\times$ is the structure of the intersection point and x, y are lengths. The energy difference in the branching plane is then

$$|\Delta E^{AB}(x, y)| = 2\sqrt{x^2 \tilde{\boldsymbol{g}}\cdot\tilde{\boldsymbol{g}} + y^2 \tilde{\boldsymbol{h}}\cdot\tilde{\boldsymbol{h}}} \tag{43}$$

or, by defining a strength or pitch (δ_{gh}) and asymmetry (Δ_{gh})

$$\delta_{gh} = \sqrt{\frac{1}{2}(\tilde{\boldsymbol{g}}\cdot\tilde{\boldsymbol{g}} + \tilde{\boldsymbol{h}}\cdot\tilde{\boldsymbol{h}})} \tag{44}$$

$$\Delta_{gh} = \frac{\tilde{\boldsymbol{g}}\cdot\tilde{\boldsymbol{g}} - \tilde{\boldsymbol{h}}\cdot\tilde{\boldsymbol{h}}}{\tilde{\boldsymbol{g}}\cdot\tilde{\boldsymbol{g}} + \tilde{\boldsymbol{h}}\cdot\tilde{\boldsymbol{h}}} \tag{45}$$

$$|\Delta E^{AB}(x, y)| = 2\delta_{gh}\sqrt{(x^2 + y^2) + \Delta_{gh}(x^2 - y^2)} \tag{46}$$

In addition, the average energy in the branching plane is given by

$$\bar{E}^{AB}(x, y) = E^\times + x(\boldsymbol{s}^{AB}\cdot\hat{\boldsymbol{x}}) + y(\boldsymbol{s}^{AB}\cdot\hat{\boldsymbol{y}}) \tag{47}$$

where $E^\times$ is the energy at the intersection point. Since only the projection of $\boldsymbol{s}^{AB}$ on the branching plane is required, we can define a relative tilt (σ) as this projection, conveniently scaled

$$\sigma = \sqrt{s_x^{\,2} + s_y^{\,2}} \tag{48}$$

$$s_x = \frac{\boldsymbol{s}^{AB}\cdot\hat{\boldsymbol{x}}}{\delta_{gh}}; \qquad s_y = \frac{\boldsymbol{s}^{AB}\cdot\hat{\boldsymbol{y}}}{\delta_{gh}} \tag{49}$$

with which the average energy is expressed as

$$\bar{E}^{AB}(x, y) = E^\times + \delta_{gh}(x s_x + y s_y) \tag{50}$$

and the energies of the two states are

$$\begin{aligned} &E^A(x, y),\ E^B(x, y) \\ &= \bar{E}^{AB}(x, y) \pm \left|\frac{1}{2}\Delta E^{AB}(x, y)\right| \\ &= E^\times + \delta_{gh}(x s_x + y s_y \pm \sqrt{(x^2 + y^2) + \Delta_{gh}(x^2 - y^2)}) \end{aligned} \tag{51}$$

or, in polar coordinates

$$\begin{aligned} &E^A(r, \theta),\ E^B(r, \theta) \\ &= E^\times + \delta_{gh} r(\sigma\cos(\theta - \theta_s) \pm \sqrt{1 + \Delta_{gh}\cos 2\theta}) \\ &r = \sqrt{x^2 + y^2};\ \tan\theta = \frac{y}{x};\ \tan\theta_s = \frac{s_y}{s_x} \end{aligned} \tag{52}$$

where r and θ are the standard polar coordinates in the branching plane with $\boldsymbol{R}^\times$ as the origin and θ_s is the tilt heading, the direction of the tilt.

In general, there is a symmetry between the energies of the two states, as it is verified that $E^A(r, \theta) - E^\times = -(E^B(r, \theta + \pi) - E^\times)$. In Figure 1 the meaning of the different parameters is graphically represented. We note that σ is defined such that, for a symmetric intersection ($\Delta_{gh} = 0$), one of the surfaces is flat along $\theta = \theta_s$ when $\sigma = 1$: $E^A(r, \theta_s) = E^B(r, \theta_s + \pi) = E^\times$. It is tempting to define a tilt angle (the angle between the red and green planes in Figure 1), but this angle would depend on the relative scale of the energy and x, y axes, so it is not well-defined. Given that σ is a dimensionless quantity, an angle $\arctan(\sigma)$ could be formally defined, but it does not represent

DOI: 10.1021/acs.jctc.6b00384
J. Chem. Theory Comput. 2016, 12, 3636−3653

any actual angle obtainable from the representation of the surfaces.

As mentioned above, the $\hat{\boldsymbol{x}}$ and $\hat{\boldsymbol{y}}$ vectors are only defined up to transpositions and changes of sign, and therefore, θ_s can change in multiples of $\frac{\pi}{2}$ and sign, and Δ_{gh} can change its sign. It is always possible to choose $\hat{\boldsymbol{x}}$ and $\hat{\boldsymbol{y}}$ in such a way that $\Delta_{gh} \geq 0$ and $\theta_s \in \left[0, \frac{\pi}{2}\right]$, this fixes unambiguously their identity and sign, except in limit cases. We have used this choice in all the examples. For a vertical intersection ($\sigma = 0$) θ_s is undefined. In a symmetric intersection ($\Delta_{gh} = 0$) any rotation of the $\hat{\boldsymbol{x}}$ and $\hat{\boldsymbol{y}}$ vectors is allowed, which makes θ_s arbitrary, depending on the particular choice of $\hat{\boldsymbol{x}}$ and $\hat{\boldsymbol{y}}$.

The model described by eq 52 is linear and assumes the $\boldsymbol{g}^{AB}$ and $\boldsymbol{h}^{AB}$ are independent of r, the distance to $\boldsymbol{R}^{\times}$; in fact, they can be obtained for any point in the branching plane as

$$\boldsymbol{g}^{AB}(r, \theta) = \frac{\delta_{gh}}{\sqrt{1 + \Delta_{gh} \cos 2\theta}} \times[\hat{\boldsymbol{x}}(1 + \Delta_{gh})\cos\theta + \hat{\boldsymbol{y}}(1 - \Delta_{gh})\sin\theta] \tag{53}$$

$$\boldsymbol{h}^{AB}(r, \theta) = \frac{\delta_{gh}\sqrt{1 - \Delta_{gh}^2}}{\sqrt{1 + \Delta_{gh} \cos 2\theta}}[\hat{\boldsymbol{y}} \cos\theta - \hat{\boldsymbol{x}} \sin\theta] \tag{54}$$

These vectors are shown in Figure 1 too; note that $\boldsymbol{s}^{AB}$ is constant and $\boldsymbol{h}^{AB}$ is always tangent to a circle around $\boldsymbol{R}^{\times}$, but $\boldsymbol{g}^{AB}$ is only perpendicular at $\theta = \frac{n\pi}{2}$. Furthermore, by approximating $\boldsymbol{f}^{AB} \simeq \boldsymbol{h}^{AB}/\Delta E^{AB}$ we obtain

$$\boldsymbol{f}^{AB}(r, \theta) \simeq \frac{\sqrt{1 - \Delta_{gh}^2}}{2r(1 + \Delta_{gh} \cos 2\theta)}[\hat{\boldsymbol{y}} \cos\theta - \hat{\boldsymbol{x}} \sin\theta] \tag{55}$$

The magnitude of $\boldsymbol{f}^{AB}$ depends only on the location in the branching plane (r and θ) and on Δ_{gh}, the other intersection parameters do not affect the derivative coupling. By choosing Δ_{gh} positive, $\boldsymbol{f}^{AB}$ will always be larger at points close to the $\hat{\boldsymbol{y}}$ axis of the branching plane ($\theta \simeq \frac{\pi}{2}, \frac{3\pi}{2}$), where it has the direction of the $\hat{\boldsymbol{x}}$ vector. Thus, the $\hat{\boldsymbol{x}}$ vector provides the direction along which nonadiabatic effects are expected to be more significant.

From eq 55 it is also verified that the line integral of $\boldsymbol{f}^{AB}$ along a closed loop surrounding $\boldsymbol{R}^{\times}$ satisfies

$$\begin{aligned} &\oint \boldsymbol{f}^{AB}\, \mathrm{d}\boldsymbol{R} \\ &= \int_0^{2\pi} f_\theta^{AB}\, \mathrm{d}\theta \\ &= \frac{1}{2}\sqrt{1 - \Delta_{gh}^2} \int_0^{2\pi} \frac{1}{1 + \Delta_{gh} \cos 2\theta}\, \mathrm{d}\theta \\ &= \pi \end{aligned} \tag{56}$$

This property can be used to confirm the existence of a conical intersection inside a small enough region, since the same integral vanishes if the loop does not enclose $\boldsymbol{R}^{\times}$.[10]

The parameters Δ_{gh}, σ and θ_s provide a full characterization of a conical intersection described by eq 52 ($E^{\times}$ and δ_{gh} are only offset and scale parameters), but a connection between them and the features that may be significant from a chemical point of view needs be established. If the surfaces described by eq 52 are represented for different values of the parameters, it can be seen that the intersections can be classified according to two criteria: (1) whether the intersection point is a minimum of the higher surface in the branching plane (peaked intersection), or there are directions θ along which the energy of the higher state becomes lower than the intersection (sloped intersection), and (2) whether there is a single preferred relaxation direction on the lower surface (single-path intersection), or there are two such directions (bifurcating intersection). This is more clearly seen when the energy is plotted versus the polar angle θ (for an arbitrary r), as in Figure 2. The intersection is sloped if the E^A, E^B curves cross the $E^{\times}$ line. Minima on the E^B curve represent preferred paths for relaxation on the lower surface, initial relaxation along other directions would be deviated toward one of these preferred ones; bifurcating intersections show two minima, single-path intersections only one. The number of minima on E^A is the same as on E^B, and they are preferred paths leading to the intersection point on the higher surface. But, if the intersection is sloped, one (or the only) of these minima is below $E^{\times}$, which means that it is actually a relaxation path on the higher surface.

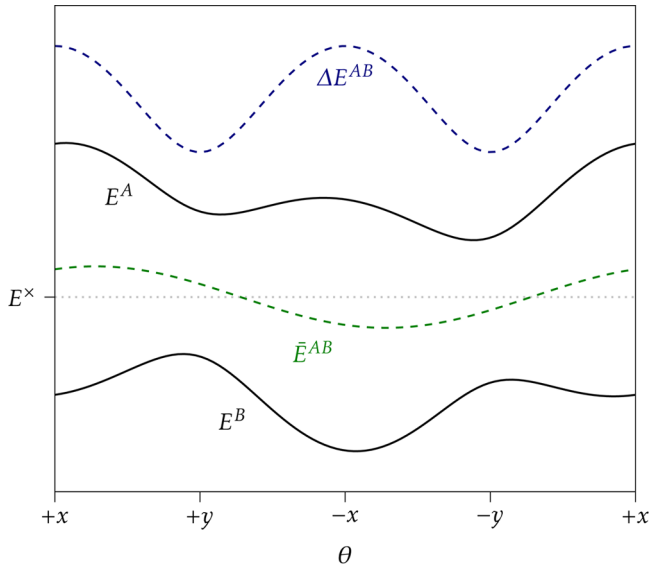

Figure 2. Plot of E vs θ for the sample intersection depicted in Figure 1 ($\Delta_{gh} = 0.5$, $\sigma = 0.3$, $\theta_s = 335°$). The energy axis is arbitrary. The dashed lines represent the energy difference and the average energy.

A similar discussion, but from a different point of view, was carried out by Atchity et al.[44] In that work, they discussed the number of straight-line paths, which corresponds to the number of stationary points (maxima, minima or inflection points with zero slope) in the E vs θ plot, and they also included an "intermediate" type of intersection, where the E^A and E^B curves touch but do not cross the $E^{\times}$ line. Thus, their patterns *P*2, *P*4, *S*2, *S*4 are equivalent, respectively, to "peaked single-path", "peaked bifurcating", "sloped single-path", "sloped bifurcating", with *P*3, *R*1, *R*2, *R*3, *S*3 being intermediate cases between them.

The conditions for an intersection being peaked or sloped, single-path or bifurcating can be found in ref 44. In terms of the parameters Δ_{gh}, σ, and θ_s, they can be stated (assuming $\Delta_{gh} \geq 0$) as

DOI: 10.1021/acs.jctc.6b00384
J. Chem. Theory Comput. 2016, 12, 3636−3653

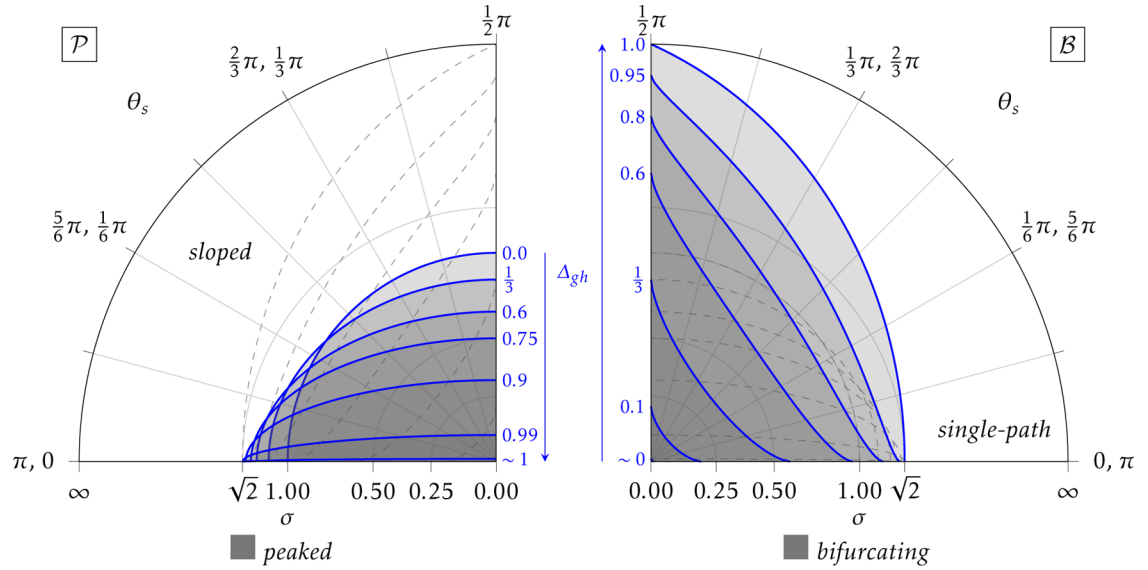

Figure 3. Representation of the conditions of eqs 57 and 58. The shaded areas correspond, for each value of Δ_{gh}, to the values of σ and θ_s for which the intersection is peaked (left panel) or bifurcating (right panel). The dashed lines are a visual aid for comparing the two graphs. Note that a nonlinear scale was used for the σ axis (radius) to allow the representation of infinite values.

$$\mathcal{P} = \frac{\sigma^2}{1 - \Delta_{gh}^2}(1 - \Delta_{gh}\cos 2\theta_s) \begin{cases} <1 & \text{peaked} \\ >1 & \text{sloped} \end{cases} \tag{57}$$

$$\mathcal{B} = \sqrt[3]{\frac{\sigma^2}{4\Delta_{gh}^2}} \times \left(\sqrt[3]{(1 + \Delta_{gh})\cos^2\theta_s} + \sqrt[3]{(1 - \Delta_{gh})\sin^2\theta_s}\right) \begin{cases} <1 & \text{bifurcating} \\ >1 & \text{single-path} \end{cases} \tag{58}$$

and they are represented in Figure 3. For large enough values of σ all intersections are sloped and single-path, and in particular every intersection with $\sigma > \sqrt{2}$ is sloped. For σ smaller than approximately Δ_{gh} all intersections are bifurcating. In general, the type of intersection depends on the specific values of Δ_{gh}, σ, and θ_s. Sloped and bifurcating intersections are only possible for $\Delta_{gh} > \frac{1}{3}$, when the dividing lines in the two panels would begin to intersect each other.

Peaked intersections are likely to act as funnels or attractors in dynamic processes occurring on the higher surface, as they are local minima, while sloped intersections could be more easily "missed", since there are continuously descending paths that avoid the intersection. Bifurcating intersections could give rise to different products once the system relaxes on the lower surface, while single-path intersections can be regarded as leading to a single product. It must be kept in mind, however, that this interpretation is based on the simple linear model described above, and is only applicable to the immediate vicinity of the intersection point: the topography of the surfaces farther away from the intersection will determine the final description. Additionally, dynamic effects would also play a role in an actual process, and this needs to be taken into account too.[5] This linear model is also limited in the type of topographies it can describe; it cannot, for example, describe 3-fold (or higher) symmetry in systems like H_3 or benzene.[46] In these cases the intersections will probably be totally symmetric ($\Delta_{gh} = 0$, $\sigma = 0$) to first order, and to go beyond this, higher-order models would be needed.[47,48]

Nikiforov et al.[49] proposed a branching plane projection method for quantitative comparisons of branching planes obtained with different methods. They use a measure based on projecting the branching vectors from one method on the plane spanned by the branching vectors from another method. Apparently, the authors use normalized $\boldsymbol{g}^{AB}$ and $\boldsymbol{h}^{AB}$ vectors as branching vectors, without orthogonalization through eqs 38−40, which in our opinion unnecessarily complicates the comparisons.

When orthonormal vectors are used to define the branching planes, the method of these authors reduces to

$$r_{IJ} = |(\boldsymbol{a}\cdot\boldsymbol{a}')(\boldsymbol{b}\cdot\boldsymbol{b}') - (\boldsymbol{a}\cdot\boldsymbol{b}')(\boldsymbol{b}\cdot\boldsymbol{a}')| \tag{59}$$

where one plane is defined by the vectors $\boldsymbol{a}$ and $\boldsymbol{b}$ and the other by $\boldsymbol{a}'$ and $\boldsymbol{b}'$, and r_{IJ} is a number that ranges from 0 for orthogonal planes to 1 for parallel planes. Incidentally, we believe there is a mistake in eq 8 in that paper, which should read

$$p_J(s_I) = (|p(\boldsymbol{a}')|^2|p(\boldsymbol{b}')|^2 - (p(\boldsymbol{a}')p(\boldsymbol{b}'))^2)^{1/2} \tag{60}$$

when this is corrected, the "BP projection" matrices reported in Table II[49] are symmetric (the projection of method A onto method B is equivalent to that of method B onto method A).

A more general analysis of the relations between subspaces, of which planes are a particular case, can be done in terms of their principal (or canonical) angles and vectors. In the specific case of two planes in N-dimensional space, two principal angles can be defined, ϕ_1 and ϕ_2, such that $\frac{\pi}{2} \geq \phi_1 \geq \phi_2 \geq 0$, and at most $N - 2$ of them are nonzero (e.g., in three dimensions ϕ_2 is always zero and a single angle ϕ_1 can be given between any two planes).[50] Assuming that both planes contain the origin, if $\phi_1 = \phi_2 = 0$, the planes are coincident, if $\phi_1 > \phi_2 = 0$, the planes intersect along a line, if $\phi_1 \geq \phi_2 > 0$, the planes are completely inclined (they only intersect at the origin), and if $\phi_1 = \phi_2 = \frac{\pi}{2}$, the planes are completely orthogonal (every vector in one plane is orthogonal to every vector in the other plane). The r_{IJ}

DOI: 10.1021/acs.jctc.6b00384
J. Chem. Theory Comput. 2016, 12, 3636−3653

number employed by Nikiforov et al. can equivalently be obtained from the principal angles:

$$r_{IJ} = \cos\phi_1 \cos\phi_2 \tag{61}$$

In general, two m-dimensional spaces are related by m principal angles (at most $N-m$ nonzero), and a single ratio can be defined as $r_{IJ} = \prod \cos\phi_i$. Furthermore, a single angle between the spaces can also be defined as $\Phi = \arccos r_{IJ}$.[51]

The principal angles and the value of r_{IJ} are independent of the choice of vectors within each plane, but if they are chosen in some consistent and well-defined way (e.g., $\hat{\boldsymbol{x}}$ and $\hat{\boldsymbol{y}}$), then it is also possible to quantify a meaningful relation between the vectors, such as the in-plane rotation needed to match the vectors of one plane with the vectors of the other plane, after the two planes are rotated to be parallel.

2.4. Conical Intersection Optimization. Any molecular structure where there is a degeneracy between two electronic states is a conical intersection (or at least an intersection of some kind[10]). In order to define and characterize specific structures, one is usually interested in MECIs, which are energy minima subject to the degeneracy between two states.

In this work the conical intersections are located and optimized using the projected constrained optimization (PCO) method.[52,53] This method allows the use of an arbitrary number of constraints, geometrical or not, as long as they can be formulated as a function of the molecular structure, $c(\boldsymbol{R}) = 0$. The value of such a function at the initial structure need not be zero, but it is requested to be zero at the optimized structure. The optimization proceeds by separating the coordinate space into two subspaces by means of a unitary matrix $\mathbf{T}$: one in which the constraints are, to first order, not modified, and another in which the constraints are modified. At each iteration the matrix $\mathbf{T}$ is computed and an optimization step is obtained in each of the subspaces: in the unconstrained subspace to minimize the energy and in the constrained space to satisfy the constraints. For more details please consult ref 53.

In principle, for locating a conical intersection it would be enough to add an energy difference constraint, $\Delta E = 0$, as it is done for crossing points between states of different spin or spatial symmetry. However, as previously noted, in a conical intersection there are two directions in which the energy difference changes linearly with the displacement. In practice, this means that including a single constraint in the optimization is not enough, once the constraint $\Delta E = 0$ is satisfied, to guarantee that it will be maintained (to first order); a second constraint is needed, and this is of course the nonadiabatic coupling.

To define the constraints in the PCO method, not only the functions $c(\boldsymbol{R})$ are needed, but their derivatives $\partial c(\boldsymbol{R})/\partial \boldsymbol{R}$. For searching conical intersections the two constraints are defined as

$$c_1(\boldsymbol{R}) = E^A(\boldsymbol{R}) - E^B(\boldsymbol{R}); \quad \frac{\partial c_1(\boldsymbol{R})}{\partial \boldsymbol{R}} = \boldsymbol{g}^A(\boldsymbol{R}) - \boldsymbol{g}^B(\boldsymbol{R}) \tag{62}$$

$$c_2(\boldsymbol{R}) = 0; \quad \frac{\partial c_2(\boldsymbol{R})}{\partial \boldsymbol{R}} = \boldsymbol{h}^{AB}(\boldsymbol{R}) \tag{63}$$

with $E^A \geq E^B$. Note that the derivative of $c_2(\boldsymbol{R})$ does not match its definition as a constant; this is simply an artificial device to ensure that the constraint is always satisfied and that the geometry is not modified along the direction given by $\boldsymbol{h}^{AB}$. Also, to avoid instabilities, the energy minimized in the unconstrained space by the PCO method is neither E^A nor E^B, but their average, $\frac{1}{2}(E^B + E^A)$.

It is not the aim of this work comparing the performance of the optimization algorithm with other methods, but we note that other methods have indeed been proposed. Some of these make use of the nonadiabatic coupling vector;[54−56] others use penalty functions[14,15] or a branching plane update.[16] For a comparison of three of these methods, see ref 57. The method used in this work has the appeal of needing very little additional implementation once the general PCO method is available and of being easy to combine with additional constraints.

3. COMPUTATIONAL DETAILS

The implementation of the nonadiabatic couplings in a development version of Molcas 8[23] was tested by optimizing conical intersections in several molecular systems. As test systems we chose those used in refs 15, 16, and 57. In all cases we used SA-CASSCF for energies, gradients and nonadiabatic couplings, the basis set, except when noted otherwise, was ANO-RCC with double-ζ-plus-polarization contraction,[58] the atomic compact Cholesky decomposition (acCD)[59] was employed in all calculations to treat two-electron integrals, with the default threshold in Molcas 8 (10^{-4} E_h). Active spaces and numbers of roots in the state average are detailed in Table 1. The active space included the full π or conjugated space, except for stilbene and the green fluorescent protein (GFP) chromophore anion, where only the central π bond was included; for ethylene and methaniminium two σ orbitals correlating with the π orbitals at the twisted geometry were added; for ketene and diazomethane two in-plane p orbitals at the terminal CO or NN atoms were added.

Table 1. Systems Studied in This Work[a]

molecule	structure	(n_e, n_o)	n_s
ethylene[60,61]	(**a**)	(6, 4)	4
ethylene	(**b**)	(6, 4)	3
ethylene	(**c**)	(2, 2)	2
methaniminium[62]	(**d**)	(6, 4)	4
methaniminium	(**e**), (**f**)	(2, 2)	2
ketene[63]	(**g**)	(6, 5)	2
diazomethane[64]	(**h**)	(6, 5)	2
butadiene[65]	(**i**), (**j**), (**k**)	(4, 4)	2
benzene[66]	(**l**)	(6, 6)	2
fulvene[67]	(**m**)	(6, 6)	2
azulene[68]	(**n**)	(10, 10)	2
s-indacene[69]	(**o**)	(12, 12)	2
PSB3[70]	(**p**)	(6, 6)	2
Me-PSB5[71]	(**q**)	(10, 10)	2
stilbene[72]	(**r**)	(2, 2)	3
GFP chromophore[73]	(**s**)	(2, 2)	2

[a] n_e, n_o, n_s: number of electrons, orbitals, and states, respectively, in the SA-CASSCF procedure. For the structures, see Figure 4.

For each of the systems we optimized at least one MECI, between the S_0 and S_1 states. In some systems several distinct structures were optimized, as listed in Table 1. We used the starting structures reported by Keal et al.[57] for the systems studied by them and, in other cases, manually distorted geometries. All starting geometries, as well as final geometries and energies are available in the Supporting Information. The convergence thresholds for the optimizations were the defaults

DOI: 10.1021/acs.jctc.6b00384
J. Chem. Theory Comput. 2016, 12, 3636−3653

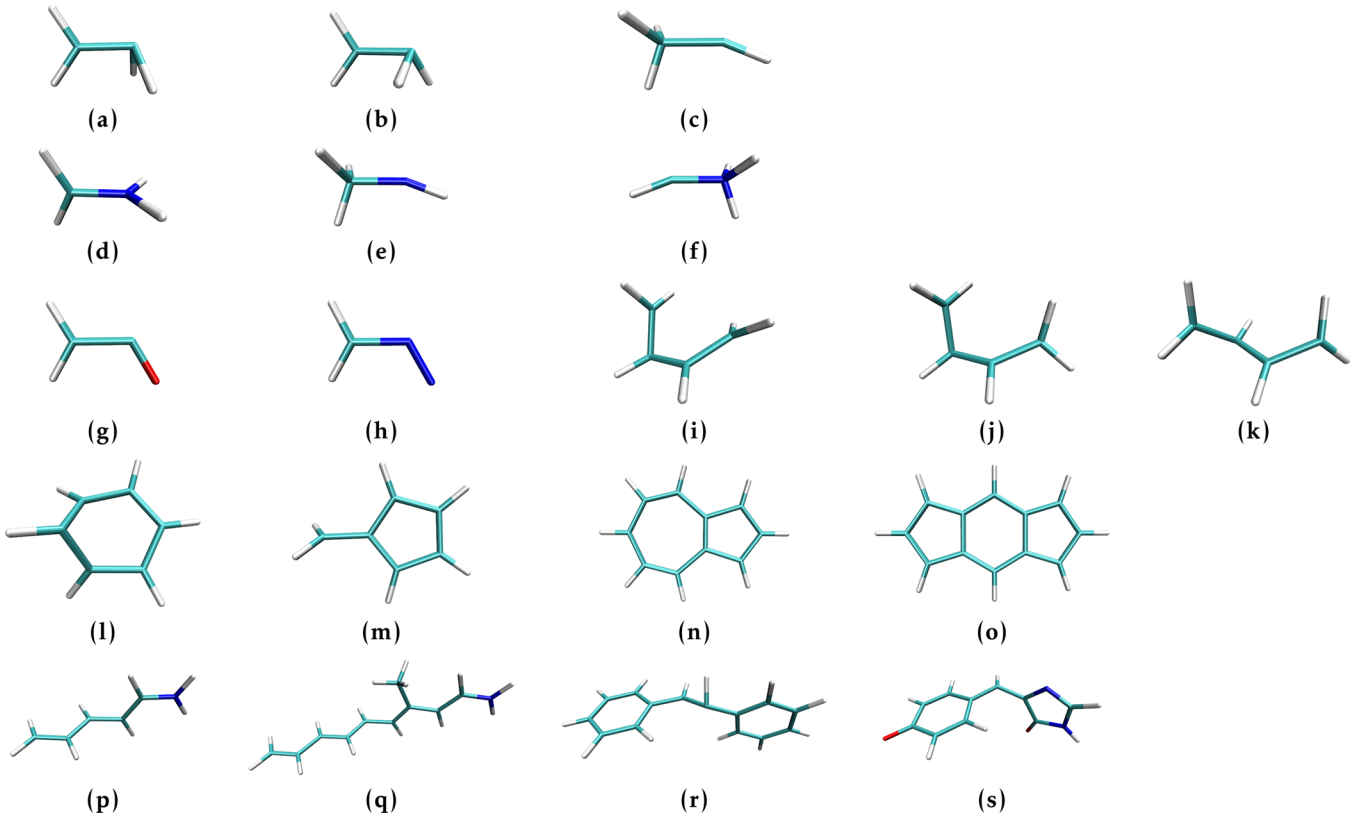

Figure 4. Structures of the optimized intersections studied in this work (Table 1).

in Molcas 8 (rms displacement and step size of 1.2×10^{-3} a_0 and 3.0×10^{-4} E_h a_0^{-1}, respectively; maximum components 1.5 times these values), plus a requirement of $|\Delta E^{AB}| \leq 10^{-5}$ E_h. No spatial symmetry was enforced in any case, although no effort was done to break the planar symmetry in the larger systems (azulene, *s*-indacene).

Once the MECI was optimized, it was characterized according to section 2.3, by computing the orthonormal $\hat{\boldsymbol{x}}$ and $\hat{\boldsymbol{y}}$ vectors that define the branching plane, as well as the pitch (δ_{gh}), asymmetry (Δ_{gh}), and tilt (σ, θ_s) of the intersection. This characterization provides a first-order model for the energies of the two intersecting states in the branching plane, eq 52. The accuracy of this model was tested by performing a series of single-point calculations at geometries on a circle in the branching plane of radius 0.001 Å, around the optimized MECI. Due to the small energy differences found in many cases, the default convergence criterion for the CASSCF calculations was tightened 1 order of magnitude.

When minimum energy paths were computed, we used the Gonzalez–Schlegel algorithm in mass-weighted coordinates.[74]

4. RESULTS AND DISCUSSION

The optimized structures of the conical intersections studied in this work are displayed in Figure 4. The number of optimization steps necessary to reach convergence, as well as the final energy difference attained, is given in Table 2.

The intersection parameters computed for the optimized structures are shown in Table 3, and the intersections are classified according to the values of $\mathcal{P}$ and $\mathcal{B}$ in Table 4. These results are obtained exclusively from the calculation of gradients and nonadiabatic coupling at the intersection point, as detailed in section 2.3. The pitch ranges from 0.01 to 0.14 E_h a_0^{-1}, the asymmetry from 0.11 to 0.88, and the relative tilt from 0.02 to 5.2, providing a wide enough spectrum of intersection topographies. As marked in Table 4, we have examples of the four basic intersection types.

In Table 5 we compare our results with the MRCI results of ref 49. In that work, the authors compared geometries and branching planes obtained with four different methods. We

Table 2. Number of Optimization Steps Required for Convergence (N_{opt}) and Final Energy Difference between the Two Electronic States (ΔE) for All the Intersections Studied in This Work

	N_{opt}	ΔE (μE_h)
(a)	14	0.16
(b)	15	1.35
(c)	25	0.09
(d)	5	0.16
(e)	18	0.15
(f)	41	0.02
(g)	11	0.55
(h)	10	0.32
(i)	16	0.22
(j)	42	0.12
(k)	34	0.20
(l)	9	0.08
(m)	21	0.04
(n)	7	0.42
(o)	6	0.53
(p)	10	1.04
(q)	44	0.87
(r)	23	0.09
(s)	32	0.06

DOI: 10.1021/acs.jctc.6b00384
J. Chem. Theory Comput. 2016, 12, 3636–3653

Table 3. Intersection Parameters for the Intersections Studied in This Work (in Atomic Units and Degrees)[a]

	$E^{\times}$	δ_{gh}	Δ_{gh}	σ	θ_s	max error (%)
(a)	−77.915980	0.0949	0.5320	0.9550	0.0	0.21
(b)	−77.916493	0.1026	0.4886	0.5668	17.1	0.27
(c)	−77.944998	0.0114	0.5114	3.3742	0.1	2.93
(d)	−94.331327	0.0687	0.4973	0.5265	90.0	1.02
(e)	−94.284472	0.0131	0.7053	1.2566	0.2	2.09
(f)	−94.270077	0.0110	0.4837	5.1882	0.0	1.42
(g)	−151.832643	0.0596	0.5279	2.0677	0.0	0.27
(h)	−147.981288	0.0536	0.7853	1.6580	0.0	0.68
(i)	−154.897265	0.1134	0.4447	0.7940	46.5	0.30
(j)	−154.890044	0.0918	0.2014	0.8563	69.9	0.40
(k)	−154.905154	0.0849	0.2782	0.7623	67.3	0.44
(l)	−230.729120	0.1249	0.3402	0.7133	90.0	0.20
(m)	−230.791851	0.1163	0.1129	0.8206	0.6	0.44
(n)	−383.598175	0.1326	0.2680	2.1588	90.0	0.76
(o)	−459.448785	0.1399	0.8753	0.4553	89.7	0.65
(p)	−248.341553	0.0614	0.3328	0.0175	52.1	1.09
(q)	−441.366313	0.0636	0.7705	0.3625	0.3	1.94
(r)	−537.322580	0.0931	0.4401	0.9439	18.8	0.31
(s)	−641.829002	0.0740	0.5441	2.0908	3.5	0.62

[a]Intersection energy $E^{\times}$, pitch δ_{gh}, asymmetry Δ_{gh}, relative tilt σ, tilt heading θ_s. "Max error" refers to the maximum difference between calculated and predicted energies (see Figure 5 and similar), relative to the energy difference.

Table 4. Condition Numbers $\mathcal{P}$ and $\mathcal{B}$ and Intersection Type Calculated According to Equations 57 and 58 for All the Intersections Studied in This Work[a]

	$\mathcal{P}$	$\mathcal{B}$	type	figure
(a)	0.60	1.07	peaked single-path	5
(b)	0.25	1.02	peaked single-path	
(c)	7.53	2.57	sloped single-path	
(d)	0.55	0.52	peaked bifurcating	
(e)	0.93	1.12	peaked single-path	
(f)	18.14	3.50	sloped single-path	
(g)	2.80	1.80	sloped single-path	
(h)	1.54	1.26	sloped single-path	
(i)	0.80	1.43	peaked single-path	
(j)	0.88	2.33	peaked single-path	
(k)	0.75	1.76	peaked single-path	
(l)	0.77	0.91	peaked bifurcating	7
(m)	0.61	2.56	peaked single-path	
(n)	6.37	2.22	sloped single-path	9
(o)	1.66	0.22	sloped bifurcating	10
(p)	0.00	0.14	peaked bifurcating	12
(q)	0.07	0.47	peaked bifurcating	
(r)	0.72	1.55	peaked single-path	
(s)	2.86	1.97	sloped single-path	

[a]Figure numbers are given for the intersections represented below.

consider MRCI as a reference and compare geometries (root-mean-square deviation, rmsd) and branching planes (cos Φ; see the end of section 2.3) for the structures studied in both works. Even though some details like basis sets, active spaces and state averaging are different, the rmsd values are generally very close or smaller than the smallest of the other methods benchmarked in ref 49, and the similarity between the branching planes is better than any of them. At least for these systems, SA-CASSCF results are a very good approximation to MRCI. Only the

Table 5. Comparison between the Results of This Work and the MRCI Results of Reference 49: rmsd between the Optimized Structures (Å) and Cosine of the Angle Φ between the Two Branching Planes (cos Φ = r_{IJ})[a]

	rmsd	cos Φ
(b)	0.0359	0.9921
(c)	0.0162	0.9958
(d)	0.0203	0.9846
(e)	0.0410	0.9927
(g)	0.0140	0.9923
(k)	0.3707	0.6641
(k′)	0.0567	0.9826
(p)	0.0409	0.9765
(r)	0.0666	0.9854
(s)	0.0966	0.9913
Averages		
SA-CASSCF[b]	0.0431	0.9882
SSR[c]	0.0551	0.7505
SF[c]	0.0696	0.8853
OM2[c]	0.1037	0.7947

[a]See text for (k) vs (k′). [b]This work, excluding (k). [c]Ref 49.

intersection (k) stands out, with both a large rmsd and relatively low cos Φ (Φ = 48.4°). Starting the optimization at the geometry of ref 49 resulted in the values reported as (k′), with a slightly higher energy (−154.894 237 E_h). The question arises whether the intersections (k) and (k′) are simply two local minima in the same intersection space or they belong to distinct spaces. We will address this question in section 4.1.

We will only discuss in some detail the first intersection (a), and we will focus on the most significant features for the rest. Figures for all the intersections are available in the Supporting Information. In Figure 5 we show a three-dimensional representation of the model surfaces generated from the parameters in Table 3. To verify their accuracy we compared the energies predicted from eq 52 with energies obtained from single-point calculations around the intersection point. The results are shown in the right panel of Figure 5. The first thing to note is that there is an almost perfect match between the model energies and the computed ones. The maximum error, relative to the energy difference, is given in Table 3 (0.21% in this case). This indicates that the calculated gradients and nonadiabatic couplings are accurate and that the first-order approximation used to define the model is appropriate, at least for the scale of displacements used (0.001 Å).

The graph shows, in accordance with Table 4, that the intersection is peaked and single-path. There is only one relaxation direction available, and that is along $-x$ on the ground-state surface. From the nature of the $\hat{\boldsymbol{x}}$ vector, it is seen that this corresponds to a planarization of the pyramidalized CH_2 group. Although the intersection is peaked single-path, it could have been sloped had σ been larger than 1.24 (the planarization would have been downhill on the excited state too), or bifurcating had σ been smaller than 0.86 (there would have been a downhill path along $+x$, possibly leading to a fragmentation of the molecule).

For this intersection, we checked that eq 56 is satisfied by computing the full derivative coupling vector $\boldsymbol{f}^{AB}$, including ${}^{\mathrm{CSF}}\boldsymbol{f}^{AB}$, at the points surrounding the optimized structure. Since the phase of the electronic states is arbitrary, there are usually spurious changes of sign in the $\boldsymbol{f}^{AB}$ vectors obtained

DOI: 10.1021/acs.jctc.6b00384
J. Chem. Theory Comput. 2016, 12, 3636−3653

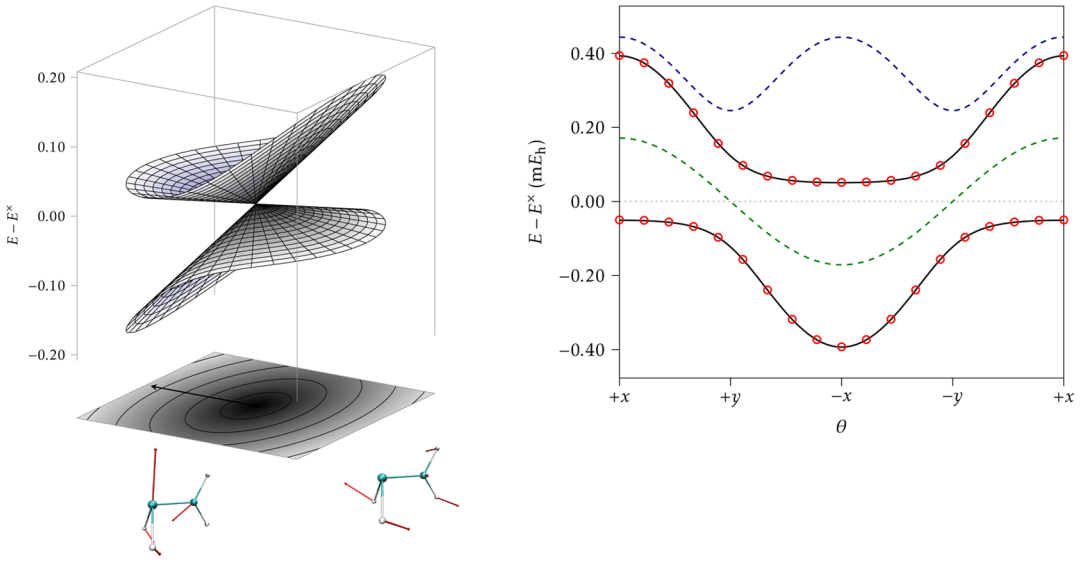

Figure 5. Representation of the symmetric ethylene (**a**) conical intersection. (left) Three-dimensional view of the two potential energy surfaces in the branching space. The bottom plane shows a contour plot of the energy difference, with an arrow representing $-\boldsymbol{s}^{AB}$ (length σ, direction $\theta_s + \pi$); the molecule pictures represent the $\hat{\boldsymbol{x}}$ (left) and $\hat{\boldsymbol{y}}$ (right) vectors, and the x and y ranges extend from −1 to +1. The color scale for the base plane is the same in all similar figures. (right) Plot of E^A and E^B around the intersection, for varying angle θ at a distance r = 0.001 Å (continuous lines); the dashed lines represent the average energy and the energy difference; the circles are the values obtained from actual single-point calculations. No fitting is involved in these figures.

from electronic structure calculations. To fix this, we used the fact that the translational and rotational components of $\boldsymbol{f}^{AB}$ are free of singularities and smoothly varying near a conical intersection; in particular, the translational component of $\boldsymbol{f}^{AB}$, due exclusively to ${}^{\mathrm{CSF}}\boldsymbol{f}^{AB}$, should be equal to $-i$ times the matrix element of the electronic linear momentum operator,[12] and the proper sign can be found unambiguously. In Figure 6 we show the results of f_θ^{AB} and f_Y^{AB} (where Y is the absolute y axis, in contrast to the $\hat{\boldsymbol{y}}$ vector defining the branching plane) and compare them with the model values from eq 56 and with the corresponding matrix elements (p_Y^{AB}), respectively. The excellent match between the two sets of values (maximum relative errors: 0.19% for f_θ^{AB}, 0.01% for f_Y^{AB}) serves to confirm the existence of a conical intersection (as the area integrates to π and not 0), the validity of the linear model for the intersection, and the accuracy of the computed derivative couplings, including the ${}^{\mathrm{CSF}}\boldsymbol{f}^{AB}$ term.

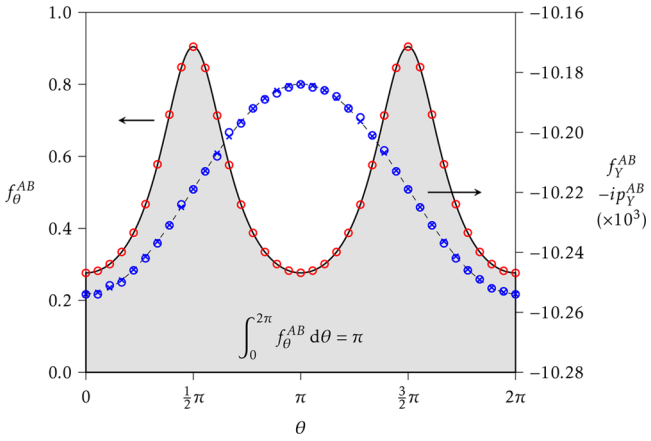

Figure 6. Values of f_θ^{AB} (red circles, left axis) and f_Y^{AB} (blue circles, right axis) for a circle surrounding the ethylene intersection (**a**). For comparison, the analytical result from the model in eq 56 is shown as a solid line, and the matrix elements of the electronic momentum operator are show with blue crosses. The area below the solid line integrates to π, a sign that there is a conical intersection inside the loop.

In order to test the sensitivity and stability of the conical intersection parameters to the basis set, we optimized (**a**) with basis set contractions of increasing size (triple-ζ and quadruple-ζ, both with polarization functions). The results are compared in Table 6, and it is seen that the topography of the intersection, as described by the parameters, does not change significantly with the basis set.

The optimized MECI for benzene is characterized in Table 4 as peaked bifurcating. The representation in Figure 7 confirms that this is the case but shows that it is very close to being single-path: the ground-state curve shows a very flat maximum in the $-y$ direction. Nevertheless, the bifurcating character is confirmed with the single-point calculations too, closely following the model curve.

Relaxation on the ground state would occur, according to the Figure 7 model, along the general $-y$ direction, but with some contribution of the symmetry-breaking $\hat{\boldsymbol{x}}$ vector. There would be thence two different minimum energy paths (MEP) connecting the MECI with possibly two different ground-state minima, although in this case it is more reasonable to presume the two paths will arrive at the same minimum structure. We computed the MEPs starting from the two minima in Figure 7 (0.001 Å from the MECI), the result for one of them is shown in Figure 8. Both the MECI structure and the ground-state minimum are symmetric, but during the MEP the symmetry is broken, which can be detected through the bond length alternation (BLA) around the ring (the difference between the sums of even and odd C−C bond lengths). In the MEP shown in Figure 8 the BLA takes positive values, getting

DOI: 10.1021/acs.jctc.6b00384
J. Chem. Theory Comput. 2016, 12, 3636−3653

Table 6. Conical Intersection Parameters for the Intersection (a) Optimized with Different Basis Set Contractions[a]

	N_{basis}	rmsd	δ_{gh}	Δ_{gh}	σ	θ_s	$\mathcal{P}$	$\mathcal{B}$
double-ζ	48	5.60	0.0949	0.5320	0.9550	0.0	0.60	1.07
triple-ζ	116	0.54	0.0929	0.5225	0.9570	0.0	0.60	1.08
quadruple-ζ	230		0.0923	0.5212	0.9702	0.0	0.62	1.10

[a]Also reported are the total number of basis functions (N_{basis}) and the root-mean-square deviation (mÅ) of the optimized geometry with respect to quadruple-ζ.

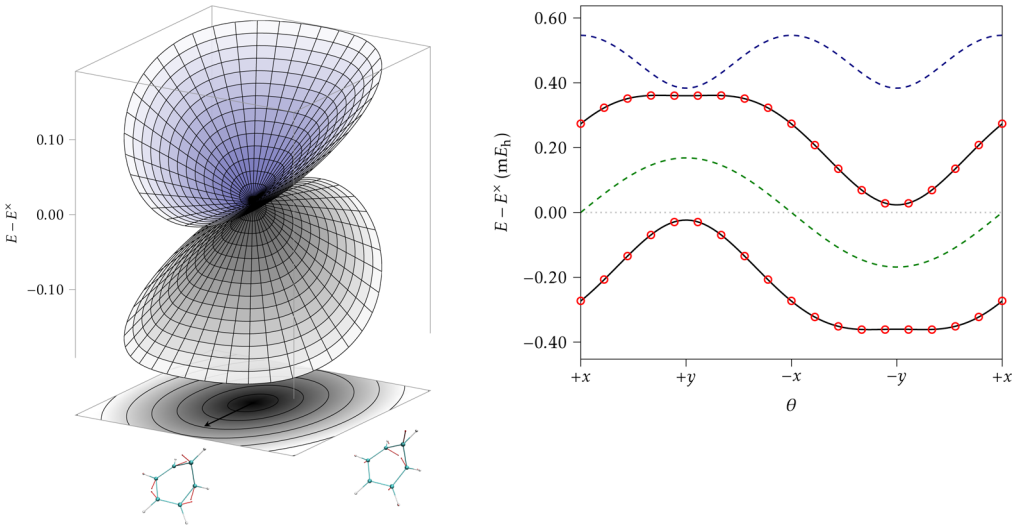

Figure 7. Representation of the benzene (1) conical intersection.

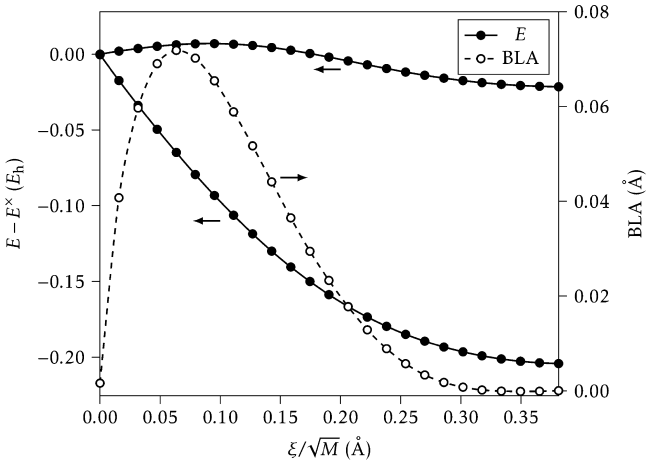

Figure 8. Minimum energy path from the benzene MECI (1), on the ground-state surface. Continuous lines show the energies of the two electronic states degenerate at the MECI, and the dashed line (open circles) shows the BLA corresponding to the structures along the MEP. The initial structure is slightly off the MECI; the horizontal axis represents the path length ξ in normalized mass-weighted coordinates (divided by the square root of the total mass).

back to zero at the final minimum; the other MEP (not shown) has the same energy values, but negative BLA.

Out of the intersections studied in this work, the one in *s*-indacene (**o**) is the only sloped bifurcating intersection (Table 4). For comparison we show the representations of azulene (**n**) and *s*-indacene (**o**) in Figures 9 and 10, respectively. The intersection in azulene has a small Δ_{gh} and large σ, while that of *s*-indacene has large Δ_{gh} and small σ, which results in a dramatic change of topography.

In both systems the structure at the MECI is symmetric. In azulene (**n**) both ground and excited state can be relaxed along the $-y$ (symmetry-maintaining) direction. In *s*-indacene only the excited state is relaxed while maintaining the symmetry, the relaxation direction for the ground state has significant contribution from the symmetry-breaking $\hat{\boldsymbol{x}}$ vector. This can be rationalized from aromaticity and antiaromaticity rules.[75] Azulene can act as an aromatic chameleon,[76] with aromatic character in both its ground state and first excited state; therefore, the two states maintain the symmetry. *s*-Indacene is antiaromatic in the ground state,[77] so it breaks the symmetry and localizes the π bonds, but it is aromatic in the excited state and can relax to a symmetric and delocalized structure.

For *s*-indacene, we computed one MEP on the ground state (the other one is related by symmetry) and one on the excited state, starting from the minima in Figure 10, the results are shown in Figure 11. On the ground state the BLA increases significantly, reaching a value of 0.637 Å at the minimum, a sign of the antiaromatic character of the electronic structure. On the excited state (inset and negative ξ in Figure 11) the minimum is found very close to the MECI, both in geometry and energy, and the BLA remains practically zero, as corresponds to the aromatic character of the excited state.

The PSB3 (protonated Schiff base with three double bonds) molecule has been used as a model for retinal, and as a benchmark system for electronic structure calculations.[78,79] The MECI topography Figure 12 is almost completely vertical ($\sigma \simeq 0$), and the $\hat{\boldsymbol{x}}$ and $\hat{\boldsymbol{y}}$ vectors represent, respectively, a change in BLA and torsion around the central bond. As for benzene (Figure 7), the intersection can be classified as peaked bifurcating, and in this case the minima on the ground-state curve are located along the $\pm x$ direction, indicating that, from the MECI, the relaxation of the BLA coordinate is preferred

DOI: 10.1021/acs.jctc.6b00384
J. Chem. Theory Comput. 2016, 12, 3636−3653

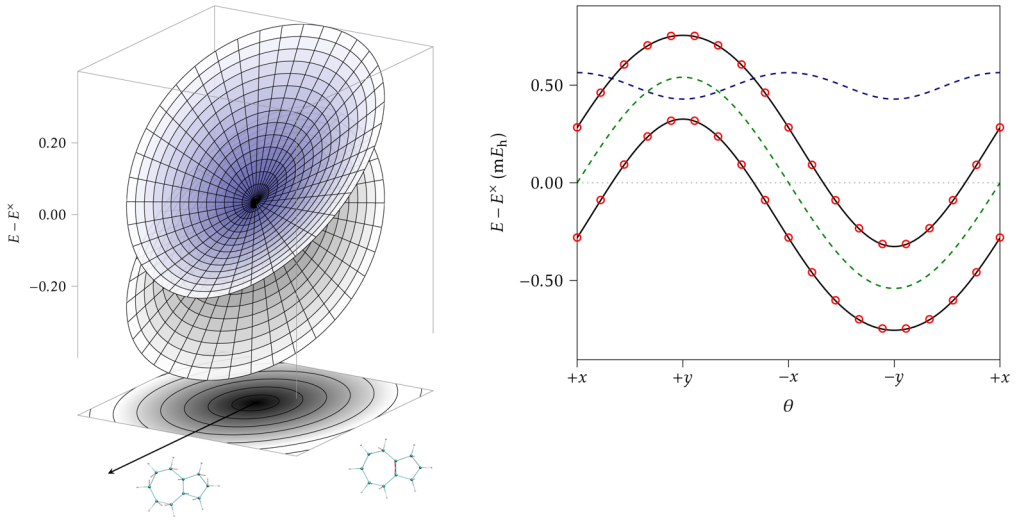

Figure 9. Representation of the azulene (**n**) conical intersection.

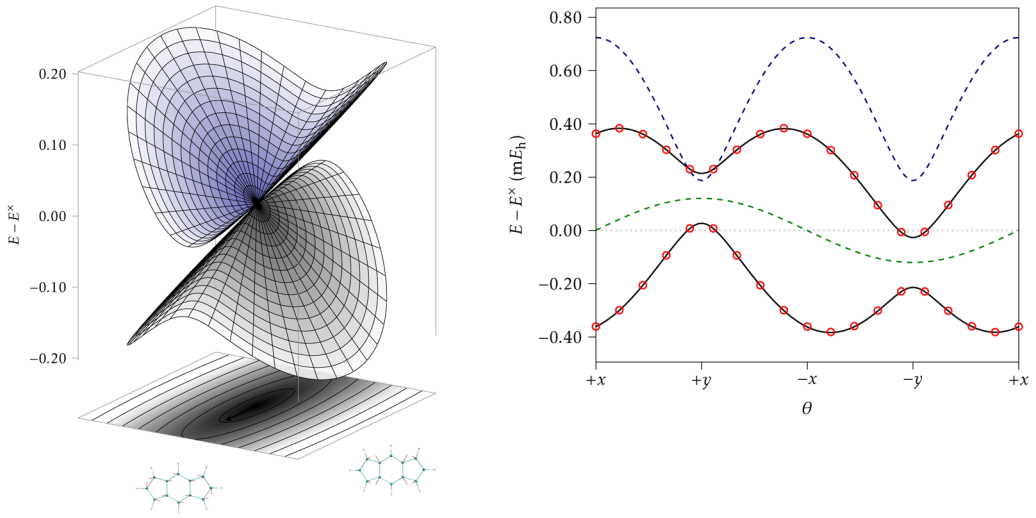

Figure 10. Representation of the *s*-indacene (**o**) conical intersection.

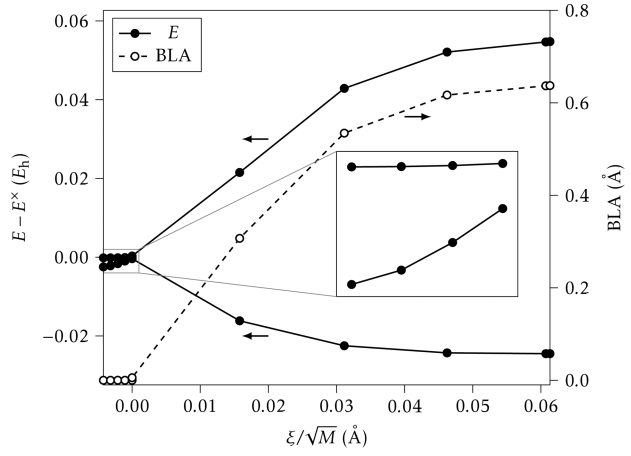

Figure 11. Minimum energy paths from the *s*-indacene MECI (**o**), on the ground-state surface (positive ξ) and excited-state surface (negative ξ and inset). See Figure 8 for further description.

over the torsion toward the cis or trans isomers. However, this relaxation, in either $+x$ or $-x$ direction, leads to a transition state connecting the cis and trans structures, and a bifurcation point must be found in the path before the transition state. Moreover, when mass-weighted coordinates are used, the $\hat{\boldsymbol{x}}$ and $\hat{\boldsymbol{y}}$ directions are scaled differently, reducing the preference for $\pm x$, since the $\hat{\boldsymbol{y}}$ vector contains larger displacements of the hydrogens. Therefore, although the initial relaxation occurs along the BLA coordinate, any realistic pathway is expected to proceed in the cis−trans axis very soon.

In Figure 13 we show two scans along the $\hat{\boldsymbol{x}}$ and $\hat{\boldsymbol{y}}$ directions from the MECI of PSB3. It can be seen that in the $\hat{\boldsymbol{y}}$ direction the linear model is a reasonably good approximation for the computed energies, but in the $\hat{\boldsymbol{x}}$ direction the curvature is significant and the linear approximation is only good for very small displacements, and at distances longer than about 0.016 Å the $\hat{\boldsymbol{y}}$ direction becomes the favored one for the relaxation of the ground state structure.

4.1. Exploring the Seam. Upon closer inspection, it turned out that the symmetric ethylene conical intersection (**a**) is not a MECI, a minimum in the intersection space, but a saddle point.[80] The average gradient $\boldsymbol{s}^{AB}$ vanishes in the intersection space (not in the branching plane), making it a stationary point, but the energy can decrease, while still maintaining the degeneracy, by distorting the geometry toward

DOI: 10.1021/acs.jctc.6b00384
J. Chem. Theory Comput. 2016, 12, 3636−3653

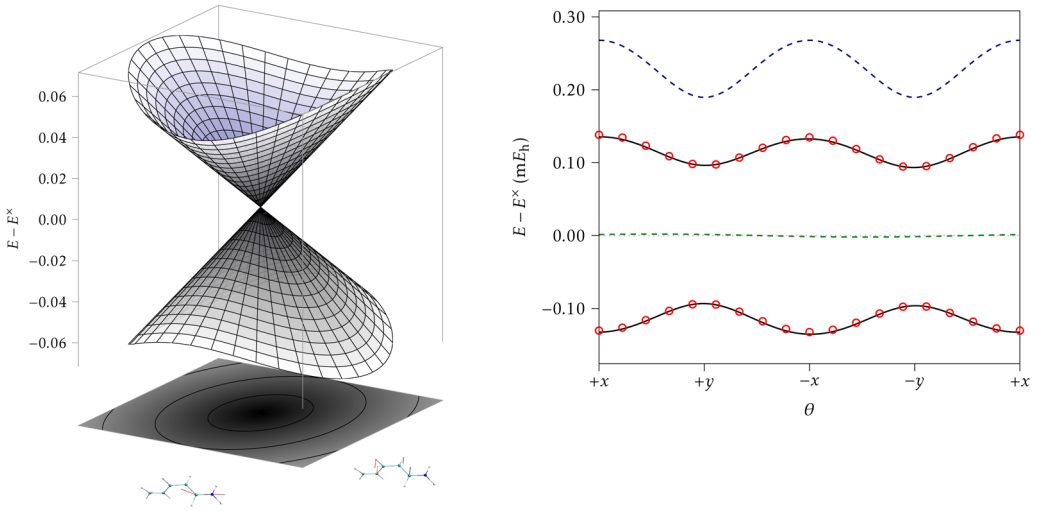

Figure 12. Representation of the PSB3 (**p**) conical intersection.

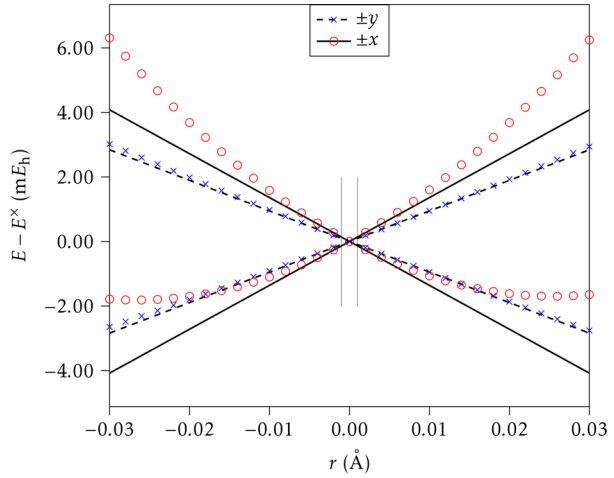

Figure 13. Energies of PSB3 along the $\hat{x}$ and $\hat{y}$ directions. The lines show the energies predicted by the linear model, circles, and crosses are obtained from single-point calculations. Vertical lines near the center show the region displayed in the right plot of Figure 12.

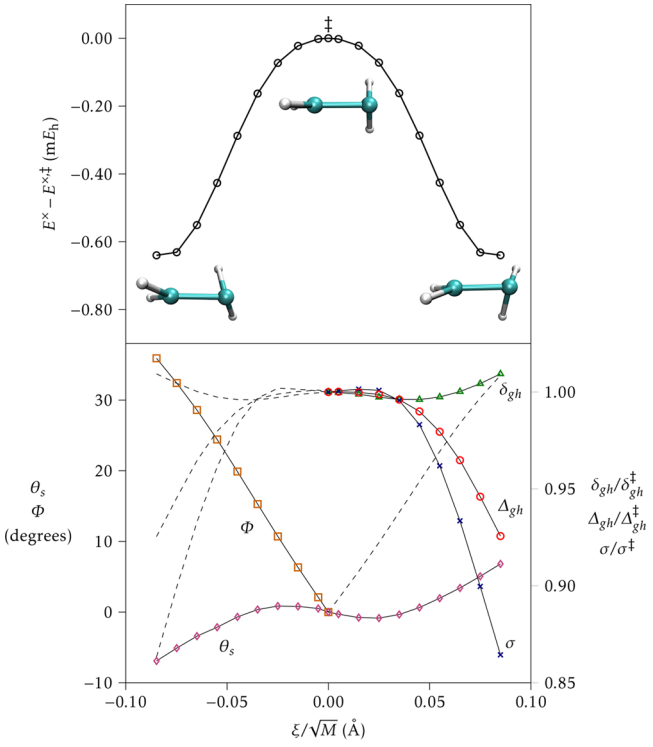

Figure 14. (top) Energy and structures along a MEP in the intersection seam starting from structure (**a**). (bottom) Conical intersection parameters along the path. To simplify the graphs, the symmetric portions have been replaced with dashed lines. **Φ** is the angle between the branching planes (see text).

the asymmetric structure (**b**) (or its specular image). This is an opportunity to explore a path in the seam or intersection space.

Starting from the (**a**) structure, we computed two MEPs in mass-weighted coordinates, with symmetry-breaking initial distortions of the pyramidalized CH_2. The MEPs were subject to the additional constraints of conical intersections (eqs 62 and 63), this is straightforward with the PCO method used for the optimizations (see also refs 81−83). This gives a set of structures in the intersection space, forming a continuous path. The results are shown in Figure 14.

The energy and significant structures are plotted in the top panel, where it is clear that the central structure (**a**), marked with ‡, is not a minimum. The structures at the left and right ends are close to (**b**), but the energies cannot be directly compared with the latter because the calculation settings are different (specifically, here we used an average of four states, while (**b**) was optimized with three states; see Table 1). The bottom panel shows the variation of the conical intersection parameters along the path. The pitch (δ_{gh}), asymmetry (Δ_{gh}), and relative tilt (σ) are shown relative to their values at the saddle point (see (**a**) in Table 3). The decrease in Δ_{gh} and σ and the increase in δ_{gh} agrees with the differences between (**a**) and (**b**) in Table 3 and are smooth and nonmonotonic (the crossing of these three lines at almost the same point is most probably fortuitous). Once the possible transpositions and sign changes of the $\hat{x}$ and $\hat{y}$ vectors are considered, the variation of θ_s is also found to be smooth and nonmonotonic and, given that the $\hat{y}$ vector is symmetry-breaking at the saddle point, if the direction of this vector is maintained, θ_s shows an antisymmetric behavior in the plot. To quantify the extent to which the branching plane, rather than the individual $\hat{x}$ and $\hat{y}$ vectors, changes, we computed the principal angles between the

DOI: 10.1021/acs.jctc.6b00384
J. Chem. Theory Comput. 2016, 12, 3636−3653

plane at each point and the plane at the saddle point.[50] In Figure 14 the "total" angle Φ[51] is represented, showing a good correlation with the path coordinate ξ.

As discussed earlier, when comparing with MRCI results,[49] at least two different transoid MECI structures can be optimized for butadiene, (**k**) and (**k**′). In order to find out if they belong to the same intersection space, we tried to find a path within the intersection that connects the two structures. We first optimized a transition state with the $\Delta E^{AB} = 0$ constraint and then computed the MEP within the intersection space, as above. The path obtained in this way did indeed connect the (**k**) and (**k**′) structures, maintaining the degeneracy at every point, and proving that the two structures are different local minima in the same intersection space. The path is represented in Figure 15. The intersection parameters and the branching

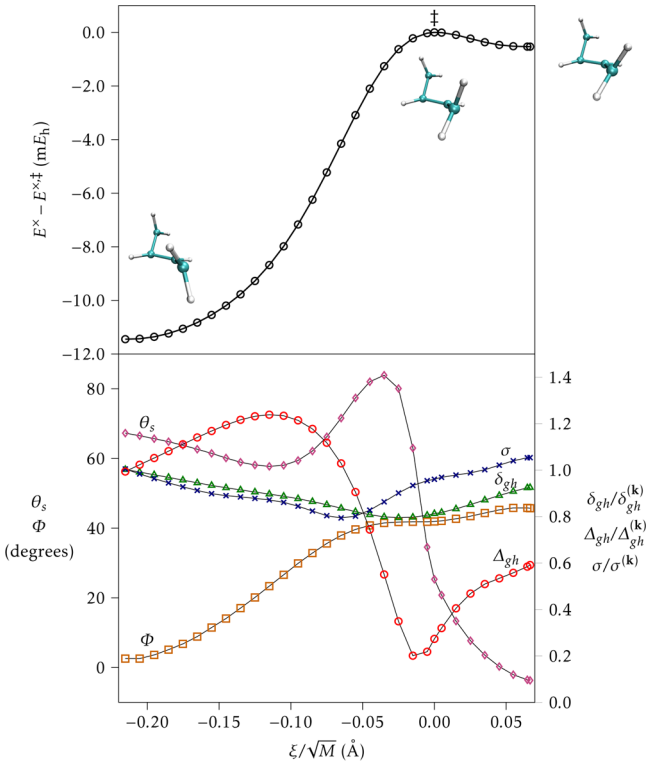

Figure 15. (top) Energy and structures along a MEP in the intersection seam connecting structures (**k**) and (**k**′). (bottom) Conical intersection parameters along the path. The parameters and the angle Φ are relative to the (**k**) structure (left side).

plane angle Φ are now computed relative to the (**k**) structure (left side), not to the transition state. The main structural difference is the rotation of a terminal CH_2 group, and the (**k**′) structure (right side) is a very shallow minimum. The change in the intersection parameters along the path is more clearly nonmonotonic, but it is still smooth.

4.2. Performance of Density-Fitted Two-Electron Integrals. It is worth reporting briefly the significance that the use of the density fitting technique for the representation of the two-electron integrals has on the overall performance and accuracy of the calculations. The systems studied in this work are not particularly demanding in terms of computational resources (they are actually quite simple), so all the calculations could be run in a regular desktop workstation (Intel i5-4670 processor, with rotating HDD, on a single core but using a 4-threaded OpenBLAS library). As a reference, the full MECI optimization for *s*-indacene (**o**), which took six geometry steps, each of them requiring one energy and three derivatives ($\boldsymbol{g}^A$, $\boldsymbol{g}^B$, $\boldsymbol{h}^{AB}$), was finished in 116 min. The same calculation with equivalent settings but with conventional two-electron integrals took 604 min, more than 5 times longer. The rmsd between the final geometries was 5.7×10^{-5} Å, and the relative differences in the final conical intersection parameters were less than 1%. More details about the impact of density fitting on specific calculation steps and on the accuracy of forces and geometries can be found elsewhere.[31,32] Given that the errors in relative energies are minimal[84−86] and, as shown again in this work, the surfaces are smooth and the gradients accurate, we see no reason to resort to conventional two-electron integrals when virtually the same results can be obtained at a fraction of the computational cost.

5. SUMMARY

We have implemented analytical derivative couplings, $\langle \Psi^B | \nabla \Psi^A \rangle$, and nonadiabatic couplings, $\langle \boldsymbol{C}^B | \nabla \mathbf{H} | \boldsymbol{C}^A \rangle$, for SA-CASSCF wave functions in Molcas. The implementation parallels closely the existing analytical gradients and is compatible with conventional and density-fitted two-electron integrals.

Nonadiabatic couplings can be used to locate and characterize conical intersections. We have optimized a set of conical intersections in different systems, using the projected constrained optimization method, and characterized them with the gradients and coupling, providing a first-order model for the two electronic surfaces near the intersection structure in the branching plane.

The systems studied are of different sizes, with active spaces ranging from (2, 2) to (12, 12). In all cases the model surfaces obtained from the characterization accurately describe single-point energies computed at 0.001 Å of the intersection point (see the errors in Table 3). This validates the use of a first-order model to represent the conical intersection topography, as well as the accuracy of the analytical gradients and nonadiabatic couplings.

The conical intersection characterization collects some information about the potential energy surfaces. We believe that a standardized definition for the conical intersection parameters and the vectors defining the branching space will allow an easier comparison of different intersections (at different structures, for different systems or computed with different methods). Depending on the values of Δ_{gh}, σ and θ_s, the intersection can be classified as peaked or sloped, bifurcating or single-path. However, this can only describe the close neighborhood to the intersection and does not consider dynamical effects that should be included in a more complete study.

■ ASSOCIATED CONTENT

Supporting Information

The Supporting Information is available free of charge on the ACS Publications website at DOI: 10.1021/acs.jctc.6b00384.

Initial geometries, final optimized geometries, $\hat{\boldsymbol{x}}$ and $\hat{\boldsymbol{y}}$ vectors, three-dimensional representations, and E vs θ graphs for all the intersections studied in this work (PDF)

DOI: 10.1021/acs.jctc.6b00384
J. Chem. Theory Comput. 2016, 12, 3636−3653

AUTHOR INFORMATION

Corresponding Author

*E-mail: Ignacio.Fernandez@kemi.uu.se.

Notes

The authors declare no competing financial interest.

ACKNOWLEDGMENTS

I.F.G., M.G.D., and R.L. acknowledge financial support from the Swedish Research Council (Grant No. 2012-3910), the eSSENCE program, and Uppsala University. This work has been supported by the Research Council of Norway (RCN) through a Centre of Excellence Grant (Grant No. 179568/V30), and T.B.P. acknowledges financial support from the RCN (Grant No. 240698/F20). F.A. gratefully acknowledges support from the FIRB "PROGRAMMA FUTURO IN RICERCA" RBFR1248UI from the Italian government.

REFERENCES

(1) *Conical Intersections*; Domcke, W., Yarkony, D. R., Köppel, H., Eds.; Advanced Series in Physical Chemistry 15; World Scientific: Singapore, 2004.

(2) Schapiro, I.; Melaccio, F.; Laricheva, E. N.; Olivucci, M. *Photochem. Photobiol. Sci.* **2011**, *10*, 867−886.

(3) Yarkony, D. R. *Chem. Rev.* **2012**, *112*, 481−498.

(4) Yonehara, T.; Hanasaki, K.; Takatsuka, K. *Chem. Rev.* **2012**, *112*, 499−542.

(5) Malhado, J. P.; Bearpark, M. J.; Hynes, J. T. *Front. Chem.* **2014**, *2*, 97.

(6) Takatsuka, K.; Yonehara, T.; Hanasaki, K.; Arasaki, Y. *Chemical Theory beyond the Born-Oppenheimer Paradigm*; World Scientific: Singapore, 2015.

(7) von Neumann, J.; Wigner, E. P. *Phys. Z.* **1929**, *30*, 467−470.

(8) Teller, E. *J. Phys. Chem.* **1937**, *41*, 109−116.

(9) Herzberg, G.; Longuet-Higgins, H. C. *Discuss. Faraday Soc.* **1963**, *35*, 77−82.

(10) Yarkony, D. R. In *Conical Intersections*; Domcke, W., Yarkony, D. R., Köppel, H., Eds.; Advanced Series in Physical Chemistry 15; World Scientific: Singapore, 2004; Chapter 2, pp 40−127.

(11) Bernardi, F.; Olivucci, M.; Robb, M. A. *Chem. Soc. Rev.* **1996**, *25*, 321−328.

(12) Yarkony, D. R. *J. Phys. Chem. A* **2001**, *105*, 6277−6293.

(13) Hammes-Schiffer, S.; Tully, J. C. *J. Chem. Phys.* **1994**, *101*, 4657−4667.

(14) Ciminelli, C.; Granucci, G.; Persico, M. *Chem. - Eur. J.* **2004**, *10*, 2327−2341.

(15) Levine, B. G.; Coe, J. D.; Martínez, T. J. *J. Phys. Chem. B* **2008**, *112*, 405−413.

(16) Maeda, S.; Ohno, K.; Morokuma, K. *J. Chem. Theory Comput.* **2010**, *6*, 1538−1545.

(17) Lengsfield, B. H., III; Saxe, P.; Yarkony, D. R. *J. Chem. Phys.* **1984**, *81*, 4549−4553.

(18) Bak, K. L.; Jørgensen, P.; Jensen, H. J. A.; Olsen, J.; Helgaker, T. *J. Chem. Phys.* **1992**, *97*, 7573−7584.

(19) Lischka, H.; Dallos, M.; Szalay, P. G.; Yarkony, D. R.; Shepard, R. *J. Chem. Phys.* **2004**, *120*, 7322−7329.

(20) Tajti, A.; Szalay, P. G. *J. Chem. Phys.* **2009**, *131*, 124104.

(21) Fatehi, S.; Alguire, E.; Shao, Y.; Subotnik, J. E. *J. Chem. Phys.* **2011**, *135*, 234105.

(22) Zhang, X.; Herbert, J. M. *J. Chem. Phys.* **2014**, *141*, 064104.

(23) Aquilante, F.; Autschbach, J.; Carlson, R. K.; Chibotaru, L. F.; Delcey, M. G.; De Vico, L.; Fdez. Galván, I.; Ferré, N.; Frutos, L. M.; Gagliardi, L.; Garavelli, M.; Giussani, A.; Hoyer, C. E.; Li Manni, G.; Lischka, H.; Ma, D.; Malmqvist, P. Å; Müller, T.; Nenov, A.; Olivucci, M.; Pedersen, T. B.; Peng, D.; Plasser, F.; Pritchard, B.; Reiher, M.; Rivalta, I.; Schapiro, I.; Segarra-Martí, J.; Stenrup, M.; Truhlar, D. G.; Ungur, L.; Valentini, A.; Vancoillie, S.; Veryazov, V.; Vysotskiy, V. P.; Weingart, O.; Zapata, F.; Lindh, R. *J. Comput. Chem.* **2016**, *37*, 506−541.

(24) Stålring, J.; Bernhardsson, A.; Lindh, R. *Mol. Phys.* **2001**, *99*, 103−114.

(25) Pedersen, T. B.; Aquilante, F.; Lindh, R. *Theor. Chem. Acc.* **2009**, *124*, 1−10.

(26) Aquilante, F.; De Vico, L.; Ferré, N.; Ghigo, G.; Malmqvist, P.-Å; Neogrády, P.; Pedersen, T. B.; Pitoňák, M.; Reiher, M.; Roos, B. O.; Serrano-Andrés, L.; Urban, M.; Veryazov, V.; Lindh, R. *J. Comput. Chem.* **2010**, *31*, 224−247.

(27) Aquilante, F.; Boman, L.; Boström, J.; Koch, H.; Lindh, R.; Sánchez de Merás, A.; Pedersen, T. B. In *Linear-Scaling Techniques in Computational Chemistry and Physics*; Zaleśny, R., Papadopoulos, M. G., Mezey, P. G., Eds.; Challenges and Advances in Computational Chemistry and Physics 13; Springer: Dordrecht, 2011; Chapter 13, pp 301−344.

(28) Aquilante, F.; Lindh, R.; Pedersen, T. B. *J. Chem. Phys.* **2008**, *129*, 034106.

(29) Boström, J.; Aquilante, F.; Pedersen, T. B.; Lindh, R. *J. Chem. Theory Comput.* **2013**, *9*, 204−212.

(30) Boström, J.; Veryazov, V.; Aquilante, F.; Pedersen, T. B.; Lindh, R. *Int. J. Quantum Chem.* **2014**, *114*, 321−327.

(31) Delcey, M. G.; Freitag, L.; Pedersen, T. B.; Aquilante, F.; Lindh, R.; González, L. *J. Chem. Phys.* **2014**, *140*, 174103.

(32) Delcey, M. G.; Pedersen, T. B.; Aquilante, F.; Lindh, R. *J. Chem. Phys.* **2015**, *143*, 044110.

(33) Page, M.; Saxe, P.; Adams, G. F.; Lengsfield, B. H., III *J. Chem. Phys.* **1984**, *81*, 434−439.

(34) Handy, N. C.; Schaefer, H. F., III *J. Chem. Phys.* **1984**, *81*, 5031−5033.

(35) Rice, J. E.; Amos, R. D. *Chem. Phys. Lett.* **1985**, *122*, 585−590.

(36) Helgaker, T.; Jørgensen, P. *Theor. Chim. Acta* **1989**, *75*, 111−127.

(37) Shepard, R. *Int. J. Quantum Chem.* **1987**, *31*, 33−44.

(38) Shepard, R.; Lischka, H.; Szalay, P. G.; Kovar, T.; Ernzerhof, M. *J. Chem. Phys.* **1992**, *96*, 2085−2098.

(39) Lischka, H.; Dallos, M.; Shepard, R. *Mol. Phys.* **2002**, *100*, 1647−1658.

(40) Helgaker, T.; Jørgensen, P. In *Analytical Calculation of Geometrical Derivatives in Molecular Electronic Structure Theory*; Löwdin, P.-O., Sabin, J. R., Zerner, M. C., Eds.; Advances in Quantum Chemistry 19; Elsevier: Asterdam, 1988; pp 183−245.

(41) Helgaker, T.; Jørgensen, P.; Olsen, J. *Molecular Electronic-Structure Theory*; John Wiley and Sons, Ltd.: Chichester, 2000; pp 36−37.

(42) Fatehi, S.; Subotnik, J. E. *J. Phys. Chem. Lett.* **2012**, *3*, 2039−2043.

(43) Subotnik, J. E.; Alguire, E. C.; Ou, Q.; Landry, B. R.; Fatehi, S. *Acc. Chem. Res.* **2015**, *48*, 1340−1350.

(44) Atchity, G. J.; Xantheas, S. S.; Ruedenberg, K. *J. Chem. Phys.* **1991**, *95*, 1862−1876.

(45) Han, S., Yarkony, D. R. In *Quantum Dynamics at Conical Intersections*; Althorpe, S. C., Worth, G. A., Eds.; CCP6 booklets; Collaborative Computational Project on Molecular Quantum Dynamics: Daresbury, 2004; pp 38−46.

(46) Varandas, A. J. C. In *Conical Intersections*; Domcke, W., Yarkony, D. R., Köppel, H., Eds.; Advanced Series in Physical Chemistry 15; World Scientific: Singapore, 2004; Chapter 5, pp 205−270.

(47) Sicilia, F.; Blancafort, L.; Bearpark, M. J.; Robb, M. A. *J. Phys. Chem. A* **2007**, *111*, 2182−2192.

(48) Yarkony, D. R. *J. Chem. Phys.* **2005**, *123*, 204101.

(49) Nikiforov, A.; Gamez, J. A.; Thiel, W.; Huix-Rotllant, M.; Filatov, M. *J. Chem. Phys.* **2014**, *141*, 124122.

(50) Björck, Å.; Golub, G. H. *Math. Comput.* **1973**, *27*, 579−594.

(51) Jiang, S. *Geom. Dedic.* **1996**, *63*, 113−121.

(52) Anglada, J. M.; Bofill, J. M. *J. Comput. Chem.* **1997**, *18*, 992−1003.

(53) De Vico, L.; Olivucci, M.; Lindh, R. *J. Chem. Theory Comput.* **2005**, *1*, 1029−1037.

DOI: 10.1021/acs.jctc.6b00384
J. Chem. Theory Comput. 2016, 12, 3636−3653

(54) Ragazos, I. N.; Robb, M. A.; Bernardi, F.; Olivucci, M. *Chem. Phys. Lett.* **1992**, *197*, 217−223.
(55) Manaa, M. R.; Yarkony, D. R. *J. Chem. Phys.* **1993**, *99*, 5251−5256.
(56) Bearpark, M. J.; Robb, M. A.; Schlegel, H. B. *Chem. Phys. Lett.* **1994**, *223*, 269−274.
(57) Keal, T. W.; Koslowski, A.; Thiel, W. *Theor. Chem. Acc.* **2007**, *118*, 837−844.
(58) Roos, B. O.; Lindh, R.; Malmqvist, P.-Å.; Veryazov, V.; Widmark, P.-O. *J. Phys. Chem. A* **2004**, *108*, 2851−2858.
(59) Aquilante, F.; Gagliardi, L.; Pedersen, T. B.; Lindh, R. *J. Chem. Phys.* **2009**, *130*, 154107.
(60) Ben-Nun, M.; Martínez, T. J. *Chem. Phys. Lett.* **1998**, *298*, 57−65.
(61) Barbatti, M.; Paier, J.; Lischka, H. *J. Chem. Phys.* **2004**, *121*, 11614−11624.
(62) Barbatti, M.; Aquino, A. J. A.; Lischka, H. *Mol. Phys.* **2006**, *104*, 1053−1060.
(63) Cui, Q.; Morokuma, K. *J. Chem. Phys.* **1997**, *107*, 4951−4959.
(64) Yamamoto, N.; Bernardi, F.; Bottoni, A.; Olivucci, M.; Robb, M. A.; Wilsey, S. *J. Am. Chem. Soc.* **1994**, *116*, 2064−2074.
(65) Olivucci, M.; Ragazos, I. N.; Bernardi, F.; Robb, M. A. *J. Am. Chem. Soc.* **1993**, *115*, 3710−3721.
(66) Palmer, I. J.; Ragazos, I. N.; Bernardi, F.; Olivucci, M.; Robb, M. A. *J. Am. Chem. Soc.* **1993**, *115*, 673−682.
(67) Bearpark, M. J.; Bernardi, F.; Olivucci, M.; Robb, M. A.; Smith, B. R. *J. Am. Chem. Soc.* **1996**, *118*, 5254−5260.
(68) Bearpark, M. J.; Bernardi, F.; Clifford, S.; Olivucci, M.; Robb, M. A.; Smith, B. S.; Vreven, T. *J. Am. Chem. Soc.* **1996**, *118*, 169−175.
(69) Bearpark, M. J.; Celani, P.; Jolibois, F.; Olivucci, M.; Robb, M. A.; Bernardi, F. *Mol. Phys.* **1999**, *96*, 645−652.
(70) Garavelli, M.; Celani, P.; Bernardi, F.; Robb, M. A.; Olivucci, M. *J. Am. Chem. Soc.* **1997**, *119*, 6891−6901.
(71) Garavelli, M.; Vreven, T.; Celani, P.; Bernardi, F.; Robb, M. A.; Olivucci, M. *J. Am. Chem. Soc.* **1998**, *120*, 1285−1288.
(72) Quenneville, J.; Martínez, T. J. *J. Phys. Chem. A* **2003**, *107*, 829−837.
(73) Martín, M. E.; Negri, F.; Olivucci, M. *J. Am. Chem. Soc.* **2004**, *126*, 5452−5464.
(74) Gonzalez, C.; Schlegel, H. B. *J. Chem. Phys.* **1989**, *90*, 2154−2161.
(75) Rosenberg, M.; Dahlstrand, C.; Kilså, K.; Ottosson, H. *Chem. Rev.* **2014**, *114*, 5379−5425.
(76) Möllerstedt, H.; Piqueras, M. C.; Crespo, R.; Ottosson, H. *J. Am. Chem. Soc.* **2004**, *126*, 13938−13939.
(77) Nendel, M.; Goldfuss, B.; Houk, K. N.; Hafner, K. *J. Mol. Struct.: THEOCHEM* **1999**, *461*−*462*, 23−28.
(78) Gozem, S.; Huntress, M.; Schapiro, I.; Lindh, R.; Granovsky, A. A.; Angeli, C.; Olivucci, M. *J. Chem. Theory Comput.* **2012**, *8*, 4069−4080.
(79) Tuna, D.; Lefrancois, D.; Wolański, Ł.; Gozem, S.; Schapiro, I.; Andruniów, T.; Dreuw, A.; Olivucci, M. *J. Chem. Theory Comput.* **2015**, *11*, 5758−5781.
(80) Freund, L.; Klessinger, M. *Int. J. Quantum Chem.* **1998**, *70*, 1023−1028.
(81) Garavelli, M.; Page, C. S.; Celani, P.; Olivucci, M.; Schmid, W. E.; Trushin, S. A.; Fuss, W. *J. Phys. Chem. A* **2001**, *105*, 4458−4469.
(82) Bearpark, M. J.; Blancafort, L.; Paterson, M. J. *Mol. Phys.* **2006**, *104*, 1033−1038.
(83) Sicilia, F.; Blancafort, L.; Bearpark, M. J.; Robb, M. A. *J. Chem. Theory Comput.* **2008**, *4*, 257−266.
(84) Boström, J.; Aquilante, F.; Pedersen, T. B.; Lindh, R. *J. Chem. Theory Comput.* **2009**, *5*, 1545−1553.
(85) Boström, J.; Delcey, M. G.; Aquilante, F.; Serrano-Andrés, L.; Pedersen, T. B.; Lindh, R. *J. Chem. Theory Comput.* **2010**, *6*, 747−754.
(86) Boström, J.; Pitoňák, M.; Aquilante, F.; Neogrády, P.; Pedersen, T. B.; Lindh, R. *J. Chem. Theory Comput.* **2012**, *8*, 1921−1928.

DOI: 10.1021/acs.jctc.6b00384
J. Chem. Theory Comput. 2016, 12, 3636−3653